Department of Physics and Astronomy

University of Heidelberg

Master thesis

in Physics

submitted by

Hannes Carsten Lindenblatt

born in Kassel

2017

Resonant Multi-Photon Ionization Experiments on Neon Monomers and Dimers Augmented by Pulse Intensity and Wavelength Diagnostics

This Master thesis has been carried out by

Hannes Carsten Lindenblatt

at the

Max-Planck-Institute for Nuclear Physics in Heidelberg

under the supervision of

Priv.-Doz. Dr. Robert Moshammer

and

Dr. Sven Augustin

Abstract

This thesis deals with experiments on resonant multi-photon double ionization of Neon monomers and dimers. Experiments were carried out at the reaction microscope beamline of the XUV free-electron laser FLASH2. Employing the variable gap undulators of FLASH2, the photon energy was scanned over the 2s-2p resonance in ionic Ne^+ at 26.9 eV, where resonance-enhanced sequential ionization and single-photon laser-enabled Auger decay (spLEAD) is expected for monomers and Interatomic Coulombic Decay (ICD) for dimers. As FLASH2 operates in SASE mode, which leads to large statistical fluctuations, post-analysis of single-shot diagnostics was developed and performed. The pulse energy was monitored through a photocurrent on the final focusing mirror and the photon energy with an electron spectrometer. Through single-shot analysis of the pulse-energy better insight into the power scaling of the ionization rates could be gained.

Zusammenfassung

Diese Arbeit befasst sich mit Experimenten zur resonanten Multiphotonenionisation von Neon-Monomeren sowie -Dimeren. Die Messungen wurden an der Reaktionsmikroskop-Beamline des XUV Freie-Elektronen-Lasers FLASH2 durchgeführt. Der 2s-2p Übergang im Ne^+ Ion bei 26.9 eV Photonenenergie konnte mit Hilfe der verstellbaren Undulatorspalten des FLASH2 abgetastet werden. Aufgrund dieses Übergangs werden bei Neon Monomeren *resonance-enhanced sequential ionization* sowie *single-photon laser-enabled Auger decay* (spLEAD) und bei Dimeren *Interatomic Coulombic Decay* (ICD) erwartet. Da FLASH2 im SASE-Modus arbeitet, und daher statistische Fluktuationen zu erwarten sind, wurden Diagnostiken für die einzelnen Pulse entwickelt und ausgewertet. Die Pulsenergie wurde dazu mittels eines Photostroms am Fokussierspiegel als letztes optisches Element und die Photonenenergie mit einem Elektronenspektrometer gemessen. Durch pulsaufgelöste Analyse der Pulsenergie konnte ein genauerer Einblick in die Skalierung von Ionisationsraten gewonnen werden.

Contents

1 Introduction

Free-electron lasers (FELs) are accelerator-based light sources, that produce short and intense light pulses in the THz to infrared [6] and XUV [9, 21] to hard X-ray regimes [22]. While FELs for long-wavelength radiation are already operational since several decades [36], short-wavelength FELs emerged only recently within the last two decades. FLASH (FEL in Hamburg), the first FEL that reached into the XUV regime became available for user operation in 2005 [9].

Short-wavelength FELs exceed the light brilliance, the product of intensity, beam divergence and spectral bandwidth, by several orders of magnitude in comparison to other types of light sources, such as synchrotrons and high-harmonic generation [52] (see Figure 1.1).

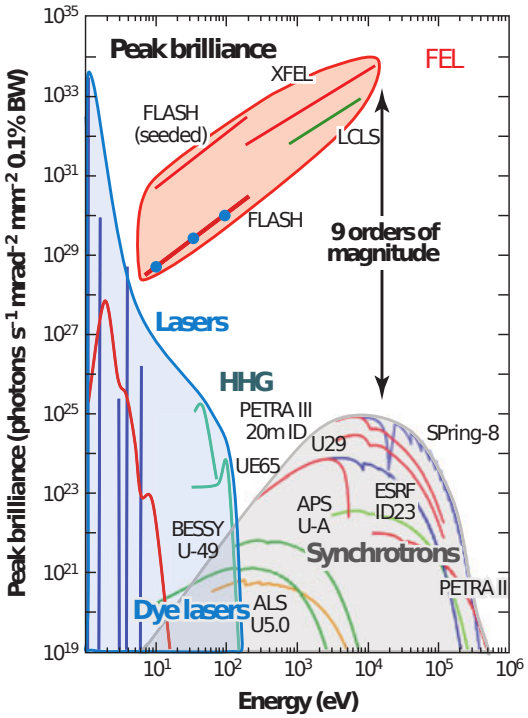

Figure 1.1: Brilliance of various light sources. FELs are the most brilliant sources, especially at high photon energies. Image taken from Reference [52].

This has enabled several new measurement techniques: Most notably single-shot diffractive imaging of nanometer sized particles [26, 28] and crystals [15], time-resolved studies through pump-probe measurements on e.g. molecular dynamics [41, 43, 44]) and multi-photon processes [46, 55] with, in this form, previously unavailable photon energies.

As the name suggests, an FEL is an amplifier for light on the basis of free electrons. These electrons have highly relativistic energies and originate from large-scale accelerator facilities. They come in form of short pulses with peak currents of a few kilo amperes. Several FEL facilities work in the so called Self-Amplified Spontaneous Emission (SASE) mode, where the overall gain in the device is such, that spontaneous emission from the early parts of the beam-path will still be amplified to the saturation limit. Due to the statistical nature of spontaneous emission this comes with some drawbacks: When the electron bunch is longer than the coherence length of the emitted light, there will be several sub-pulses with a random phase difference forming a total pulse. Also there is a large fluctuation of the total pulse intensity, which in fact gains in variance, as the pulse durations decrease [29]. These properties make studies difficult, when only average pulse characteristics are available, but observables correlate strongly with more than one of those. Therefore, it becomes necessary to characterize the single shots of the FEL to correctly account those correlations.

FELs can also be operated in seeded mode in order to overcome the limitation due to statistical fluctuation from SASE. This also gives the pulses full temporal coherence. A lower-intensity laser pulse is provided from another source and fed into the FEL. Control over the light properties of the seeding laser thereby allows control of the resulting output light, but typically the seed laser itself is already a complex device and stable synchronized operation with the FEL is challenging. Nevertheless, it was demonstrated and is available for user operation at FERMI in Trieste [4]. While optical lasers are capable of generating seed pulses for XUV FELs by using high harmonics of the fundamental laser wavelength, this concept fails for hard X-ray FELs because external hard X-ray seed pulses do not exist. However, the so-called self-seeding method, where the FEL is seeded by a portion of its own beam split off by a diamond crystal, has been demonstrated for hard X-rays [5].

FLASH has been upgraded in 2016 by adding a new undulator line and experimental hall, the FLASH2 project. The Max Planck Institute for Nuclear Physics (MPIK) has set up and commissioned the first permanent endstation at FLASH2, a reaction microscope (Remi), equipped with a split- and delay-unit for XUV pump-probe experiments. Since a Remi is capable of tracking the ionization products of every single FEL pulse it is important to track key parameters, like pulse energy and wavelength fluctuations on a shot-to-shot basis. To this end, FLASH provides gas monitor detectors (GMD) and the OPIS, a photo-electron spectrometer.

In this work, the influence of pulse- and photon-energy on multi-photon double ionization via resonance-enhanced sequential ionization or single-photon laser-enabled Auger decay (spLEAD) of atomic neon as well as the resonantly-

enhanced interatomic Coulombic decay (ICD) [19] in neon dimers is investigated by observation of ion production rates. In order to gain insight in those processes, single-shot pulse-diagnostics are analysed in order to overcome the limitations due to the statistical fluctuations of the SASE FEL mode.

A brief introduction into the theoretical background of these processes is given in Section 2. An overview of the key experimental components for this work is described in Section 3. The developed and/or utilized analysis methods are presented in Section 4. And finally the performance of the diagnostics and the found results on neon is discussed in Section 5.

2 Multiphoton-Ionization Pathways

There are several mechanisms to be considered for multi-photon ionization. The most prominent will be compiled in the following from References [17, 30, 40, 45]. The processes expected for atomic neon and neon dimers in this work are summarized in Section 2.7.1.

2.1 Direct Multi-Photon Ionization

Direct multi-photon ionization means an electronic transition from a bound energy eigenstate to the unbound continuum through means of intermediate non-eigenstates. Those have a very short lifetime imposed by Heisenberg's uncertainty limit. Therefore, it requires all involved photons in a quasi-instantaneous moment and thus the ionization yield Y scales with Intensity like

$$Y(I) = \sigma I^n \,, \tag{2.1}$$

where n is the minimum number of photons required to overcome the ionization threshold[45, p. 11].

2.2 Strong-Field Ionization

Strong-field ionization refers to a regime, where the electric field of the light is comparably strong to the nuclear field. In the time average, electrons gain additional energy from movement in the oscillating field. This is the so called ponderomotive potential

$$U_p = \frac{1}{2} m_e \left\langle v^2 \right\rangle_t = \frac{e^2 \epsilon_0^2}{4 m_e \omega^2} = \frac{e^2 I}{2 \varepsilon_0 c m_e \omega^2} \,, \tag{2.2}$$

where ω is the angular frequency of the light field, ϵ_0 the electric field amplitude, m_e the electron rest-mass, ε_0 the vacuum permittivity and e the elementary charge. Processes in strong fields are characterized by the ratio of this ponderomotive potential and the ionization potential E_I through the so-called Keldysh parameter

$$\gamma = \sqrt{\frac{E_I}{2U_p}} = \sqrt{\frac{\varepsilon_0 c m_e E_I \omega^2}{e^2 I}} \,. \tag{2.3}$$

When the Keldysh parameter is smaller than 1, the potential is bent strongly and the electron may tunnel out of the atomic potential well. However, as the parameter scales linearly with the light frequency and only with the

square root of the inverse intensity, intensities need to be very high for high photon energies to get values below 1. Therefore, tunnel-ionization is not to be expected in the XUV regime.

2.3 Resonance-Enhanced Sequential Ionization

Resonance-enhanced sequential ionization is similar to direct multi-photon ionization, but differs such that intermediate states are energy eigenstates accessible to the electron via dipole transitions. This can greatly enhance ion yields, as the resonant absorption cross-section is higher. Furthermore if the intermediate eigenstate has a long decay time, the atom can *store* energy for this time and be ionized by photons in later parts of the light pulse. It could for example be demonstrated in three-photon double ionization of argon in Reference [39].

2.4 Auger Decay

Auger decay is an electron correlation process where an atom or ion has an inner-shell vacancy which can be filled by one electron while releasing enough energy for another electron to be ionized from the system. Typically, this occurs after ionization with high-energetic photons, as absorption cross-sections for inner-valence ionization are higher than for outer-valence, when energetically allowed.

2.5 Interatomic Coulombic Decay (ICD)

Interatomic Coulombic Decay (ICD) is another electron correlation process similar to Auger decay, but at longer interaction range in atomic and molecular clusters. It was proposed 1997 by Cederbaum, Zobeley and Tarantelli in Reference [13]. It is applicable if there is an inner-shell vacancy that can be filled by an electron, which releases enough energy to ionize another electron at a different site of the molecule or cluster. The energy transfer takes place through exchange of a virtual photon. If there is also a competing Auger decay possible, ICD is usually dominated by that channel, as the decay widths scale with the Coulomb potential. Therefore, lifetimes become longer for exchange of virtual photons with distant partners. If Auger decay is energetically not allowed, ICD provides a channel, which is very sensitive to the environment of the atom. It is also possible to initialize this process by resonantly exciting one of the atoms in the molecule, which will then transfer its energy with some delay and ionize another constituent.

2.6 Laser-Enabled Auger Decay (LEAD)

Laser Enabled Auger Decay is a modified Auger decay, where the energy of the relaxation process is initially not enough for ionization. It becomes enabled by the presence of a laser field from which one or several photons are absorbed in order to collect the missing energy to overcome the ionization threshold. It was first reported with the use of an infrared laser in double ionization of argon in Reference [40] and is described in theory in the same work. If there is only one photon necessary, one also speaks of single photon LEAD (spLEAD). This case was proposed as a sensitive tool for hole-migration dynamics in Reference [17] and only recently reported in Reference [32] for double ionization of atomic neon.

2.7 Neon Photoionization Around 27eV

2.7.1 Double Ionization of Neon Atoms

For double ionization of neon with multiple photons of approximately 27 eV there are three pathways to be considered. They have in common a direct single-photon ionization of the atomic neon (see Figure 2.1).

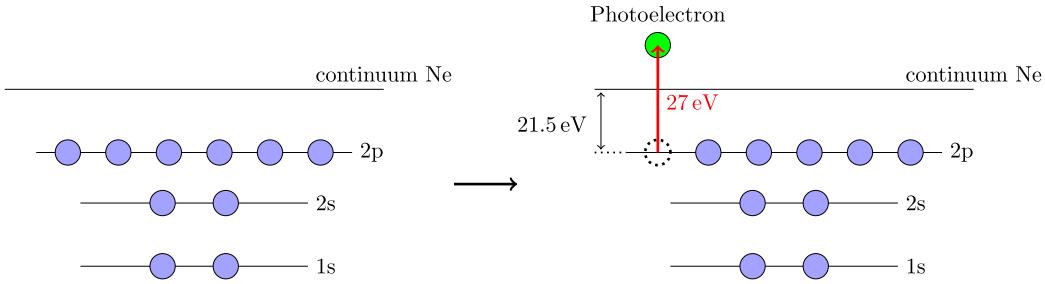

Figure 2.1: Initial single ionization of Neon. An outer-valence electron is removed and gains a kinetic energy of $\approx 5.5\,\mathrm{eV}$. Figure adapted from Reference [38].

The ionization threshold is 21.56 eV, so only ionization to the ionic ground-state $2s^2 2p^5\ {}^2P_J$ configuration is possible, which has a fine-structure splitting of 0.097 eV. With this, a photo electron with $\approx 5.5\,\mathrm{eV}$ kinetic energy is emitted. The next step is different for the three pathways. One possibility is direct two-photon ionization of a 2p electron without support of intermediate states (see Figure 2.2).

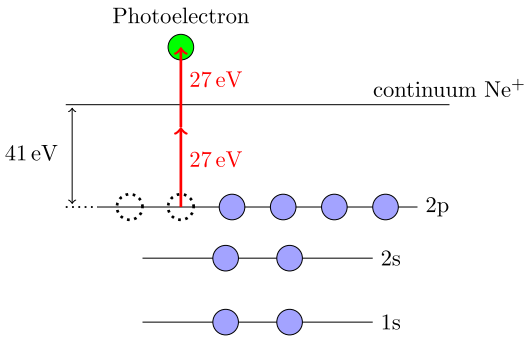

Figure 2.2: Direct multi-photon ionization of the singly charged neon ion. Figure adapted from Reference [38].

With this we arrive at the doubly charged ion in the $2s^2 2p^4\ {}^3P_J$. Another path is sequential ionization via the intermediate state $2s^2 2p^4 3s\ {}^4P_J$ with energy 27.2 eV and then direct ionization of the 3s electron (see Figure 2.3).

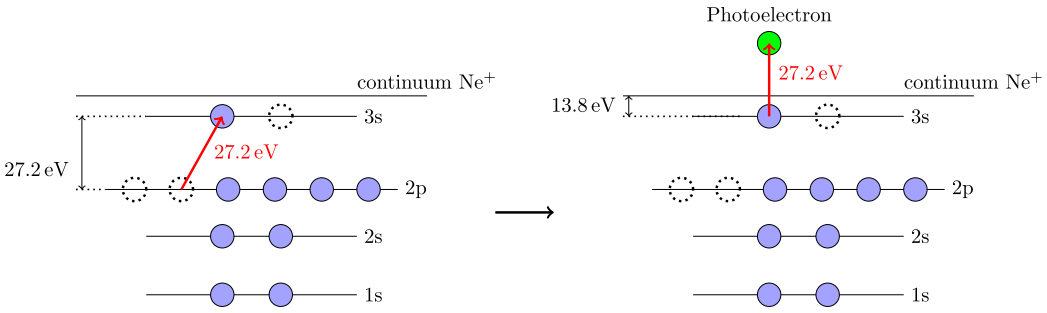

Figure 2.3: Resonance-enhanced sequential ionization of Ne^+. In the first step, a 2p electron is excited to the 3s state at 27.2 eV, then it can be expelled from this state to the continuum. Figure adapted from Reference [38].

The third way is via the $2s2p^6\ {}^2S_{1/2}$ state at 26.9 eV. From here, ionization can take place via spLEAD. One of the 2p electrons relaxes to 2s and shares the energy with another 2p electron, which can ionize with the additional help of another photon (see Figure 2.4).

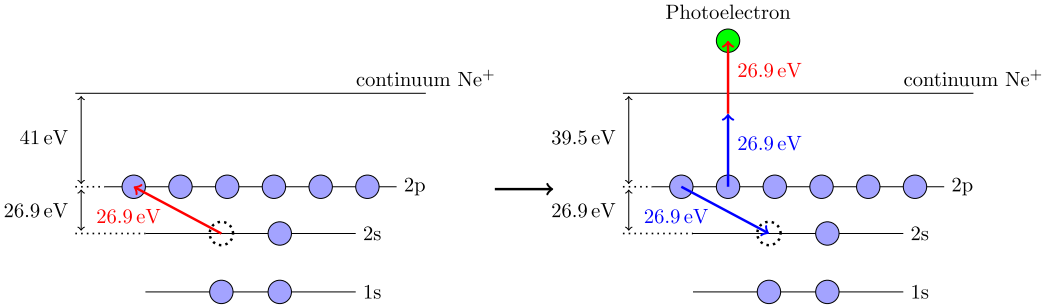

Figure 2.4: Single-photon laser-enabled Auger decay (spLEAD) in neon prepared by resonant excitation of a 2s electron to a 2p state. When another photon is absorbed by one 2p electron and another one relaxes to the 2s state, the first one can be ionized. Figure adapted from Reference [38].

In all cases, three photons are needed to produce doubly charged neon ions. Level energy values are taken from Reference [35] and visualized in Figure 2.5.

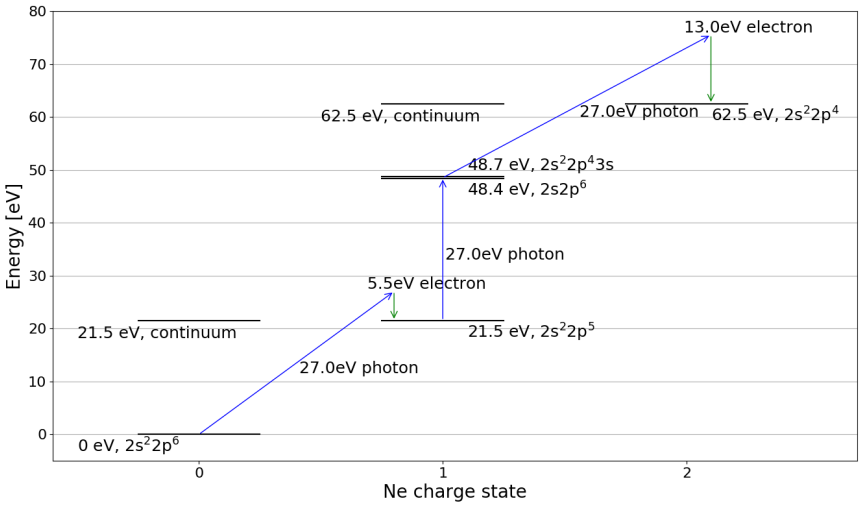

Figure 2.5: Energy levels in neon considered for ionization pathways. States and energy values are taken from *NIST Atomic Spectra Database (ver. 5.3)* [35].

2.7.2 Double Ionization of Neon Dimers

The pathways for neon dimers at 27 eV are discussed in Reference [38], which also deals with data from the same experimental campaign as the work presented here. The first step for the dimers is also direct-single photon ionization on one of the atoms. The next step can either be again direct

single-photon ionization, but of the other atom or the ion from the first step can be resonantly excited, similarly to the case before, from $2s^2 2p^5$ to $2s2p^6$ at 26.9 eV or $2s^2 2p^4 3s$ at 27.2 eV. In either case this excitation energy is sufficient to open the ICD channel for ionization of the other atom. In both pathways, two photons are necessary to ionize both the atoms and the dimer will afterwards fragment due to Coulomb repulsion. As those fragments rapidly gain decent amount of kinetic energy from this, one speaks of Coulomb explosion. Note that the total yield will increase, when the resonance is matched with the photon energy.

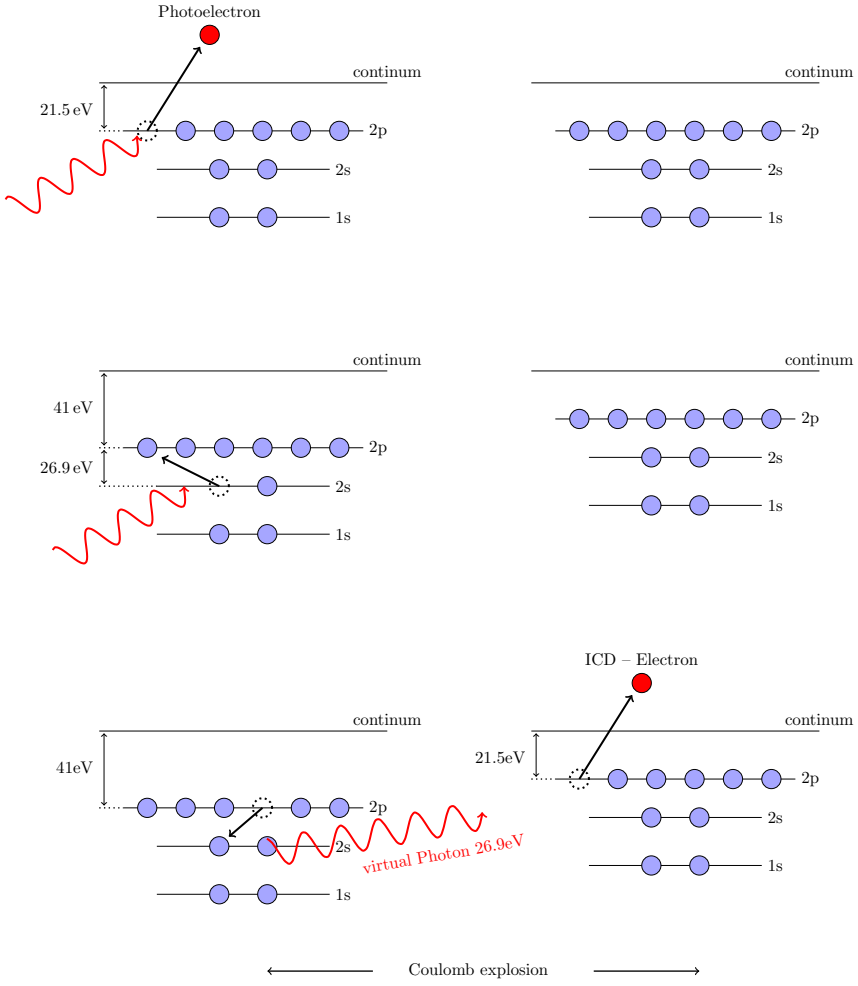

Figure 2.6: Schematic of the resonant ICD pathway in ionization of neon dimers at 26.9 eV. First one atom is ionized, then the ion is excited and finally the ion relaxes while ionizing the other atom via exchange of a virtual photon. After both atoms are ionized, the dimer fragments in a Coulomb explosion. Figure taken from Reference [38].

3 Setup

In order to perform multi-photon experiments in the XUV regime, special requirements regarding high photon energies and high intensities have to be fulfilled by the light source. If, in addition narrow resonances are to be observed, the photon energy bandwidth needs to be small. These demands are so far only matched by Free-Electron Lasers (FEL), which are described in Section 3.1. For identification of the ions created by photoionisation and their associated momenta, a so-called Reaction Microscope (Remi) is used. It is described in Section 3.2. This versatile tool is not utilized in its full capacity for the analysis done in this work. As the light delivered by the used for this work, shows large statistical fluctuations (see Section 3.1), it is imperative to observe properties of every pulse with suitable diagnostics in order to be able to analyze the potentially rare events. Here, the diagnostics described in Section 3.3 were utilized.

3.1 Free-Electron Laser / FLASH2

Free-electron lasers (FELs) are based on large-scale accelerator facilities providing bunches of highly relativistic electrons. They evolved as a successor to modern synchrotron facilities combining the accessibility of high intensities and photon energies of a synchrotron with pulse properties more similar to classical lasers (from: Light Amplification by Stimulated Emission of Radiation). However, FELs differ quite a lot from the both. In comparison to regular lasers, the amplifying medium is not a composite and usually complex material structure with discrete electric transitions, which are driven by the stimulation from the amplified light. Instead it is a gas of charged elementary particles, the eponymous electrons, with a continuous spectrum of energies. These are forced by magnetic fields on a periodic motion transverse to the beam direction. Appropriate choices for this trajectory allow coherent transfer of the electrons' kinetic energy to a light field with matching periodicity. As there is no discrete transition exploited for the gain, the accessible wavelength range of the emitted radiation is continuous and has no fundamental lower limit. Detailed descriptions of FELs and their working principle can be found in References [29, 34, 37, 42]. Here, only a short summary will be given.

The FEL consists of three main components. The electron source, the accelerator and the undulator.

Electron Source The electron bunch is produced from a special solid state component, which is irradiated by a intense short-pulse laser. With this a

cloud of electrons is expelled from the solid in a short time. The electrons are immediately accelerated in a pre-accelerator towards the main accelerator. With this, an expansion of the electron cloud due to Coulomb repulsion can be reduced because of relativistic time-dilation.

Accelerator The main accelerator of an FEL is typically a linear accelerator, as this prevents energy loss from unwanted synchrotron radiation before the target energy is reached. At FLASH, this is done with a superconducting radio-frequency-cavity linear accelerator, which was developed in the TESLA[1] collaboration [21]. Besides increasing the electron kinetic energy to the target value, there are multiple dispersive elements in order to compress the bunch length. This needs to be done, since a high peak current is essential for achieving high photon gains and short pulse durations [29].

Undulator In the undulator the kinetic energy of the electrons is converted to the desired radiation. It consists of an arrangement of permanent magnets in such a way, that the electron beam path is modulated by the Lorentz force to a sinusoidal trajectory in one transverse plane (for producing linearly polarized light) or in both transverse planes (for elliptical polarization).

The production of light can be explained in a simple picture as follows: When viewed from downstream, the electrons movement in transverse direction corresponds to a simple electric dipole oscillating with frequency $f_e = v/\lambda_u$, where λ_u is the magnetic field wavelength inside the undulator. When transforming the coordinate system to the rest-frame of the electron in longitudinal direction, the undulator period is shortened by Lorentz contraction $\lambda'_u = \lambda_u/\gamma$, with $\gamma = 1/\sqrt{1-\beta^2}$ and $\beta = v/c$. So in this frame of reference, the electrons are oscillating with frequency

$$f'_e = \frac{v \cdot \gamma}{\lambda_u} = \frac{\beta \cdot \gamma}{\lambda_u \cdot c} \tag{3.1}$$

in transverse direction and thus emit radiation at this frequency $f'_{\mathrm{ph}} = f'_e$ in the usual dipole $\sin^2\theta'$ intensity pattern, where θ' is the angle to the beam axis. When transforming back to the lab system, two effects are beneficial for the light source. First, the frequency increases by another factor of $\gamma(1+\beta)$ due to the relativistic Doppler Effect, which results in

$$f_{\mathrm{ph}} = \frac{\beta(1+\beta) \cdot \gamma^2}{\lambda_u \cdot c}\,. \tag{3.2}$$

[1] TeV-Energy Superconducting Linear Accelerator

And second, the intensity distribution gets narrower, as the angle contracts to $\theta = \theta'/\gamma$ (see also Figure 3.1).

(a) $\beta = 0$ (b) $\beta = 0.9$

Figure 3.1: Angular radiation power distribution for an electric dipole oscillating in vertical direction (a) at rest in horizontal and (b) moving with 90 percent of the speed of light to the right. Images taken from [42].

Typical values for γ are above 1000, which means $\beta \approx 1$. With this we get a photon wavelength of

$$\lambda_{\text{ph}} = \frac{c}{f_{\text{ph}}} = \frac{\gamma^2}{2\lambda_u} \,. \tag{3.3}$$

A more detailed derivation (for example in [42]) considering the electron trajectory more accurately yields the more general expression

$$\lambda_{\text{ph}} = \frac{\gamma^2}{2\lambda_u}\left(1 + \frac{K^2}{2}\right) \text{ with } K = \frac{eB_0\lambda_u}{2\pi m_e c} \,. \tag{3.4}$$

Here K is the so called undulator parameter, B_0 the magnetic field amplitude and m_e the electron mass. The undulator parameter also gives an estimate of the light cone opening

$$\theta_{\text{max}} = \frac{K}{\gamma} \,. \tag{3.5}$$

When $K \leq 1$, the light cone is narrow enough to concentrate the emitted intensity on the electron trajectory, in order to efficiently transfer energy from the electrons to the light. If this condition is fulfilled, the FEL can be operated in a mode called Self-Amplified Spontaneous Emission (SASE). The resulting photon wavelength or energy can therefore be influenced either by the electron γ factor, the undulator wavelength λ_u or parameter K which is additionally depending on the magnetic field B_0.

Self-Amplified Spontaneous Emission As for any amplifier it is necessary to provide an initial state to amplify in amplitude. This could be done by seeding the FEL with radiation from a regular laser or, for shorter wavelengths, from higher harmonics of those. But this is technically difficult,

as the relative phase between the laser pulse and the electron bunch has to be very stable. Instead, one can rely on Self-Amplified Spontaneous Emission (SASE). This means that spontaneously emitted light is further amplified in the undulator. The process of energy transfer from the electrons to the light field is nicely described in Reference [37] with a small set of four coupled differential equations. When the length of the electron bunch l_e is longer than the coherence length of the SASE light l_c, several sub-pulses can be produced by those electrons. Therefore longer electron bunches will in average produce longer composite photon pulses. One can also show a connection between the ratio of those and the fluctuation of the total pulse energy (see Reference [29]):

$$\frac{\sigma_\mathrm{E}}{E} = \sqrt{\frac{l_\mathrm{c}}{l_\mathrm{e}}}\,. \tag{3.6}$$

As a photon pulse originating from a SASE FEL is build from a random number of photon modes each with random frequency, phase and relative intensity (within respective distributions derived from the spontaneous emission), the need to observe the properties of each pulse by suitable diagnostics arises (see Section 3.3).

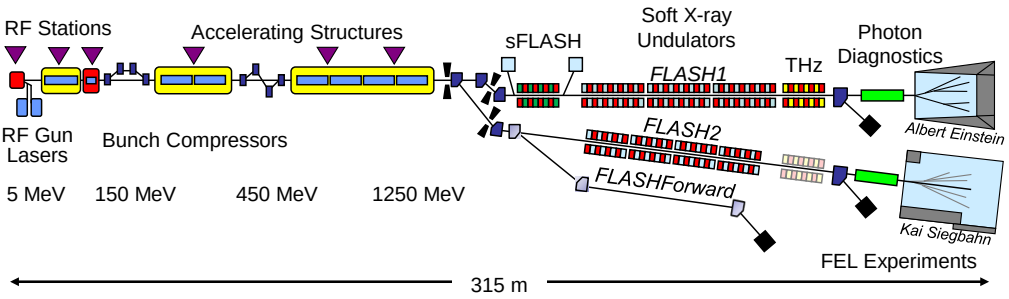

Figure 3.2: Layout of the FLASH facility. The electron source is located in the far left. Electron bunches are than accelerated and compressed in the linear accelerator. After this they are distributed to the undulator sections of FLASH1 or FLASH2, where light is produced via the SASE-FEL scheme. After the undulator section, the electron beam is dumped and photons are delivered to experiments. Image taken from [25].

FLASH2 Experiments for this work were performed at FLASH2 which is an upgrade of the Free-electron LaSer in Hamburg (FLASH). It uses electrons from the same accelerator as FLASH1, but in contrast has undulators with magnets movable in transverse direction. This does not change λ_u, but changes K as the magnetic field amplitude B_0 varies with the gap distance

between magnets (see Equation 3.4). This allows fast changes of photon energies without expensive (in terms of invested time) re-tuning of electron energies via accelerator settings. Both undulators produce linearly polarized light in horizontal direction. The accelerator supplies trains of bunches at a rate of 10 Hz. Some key parameters are compiled in Table 1 from Reference [23].

Table 1: Selection of FLASH2 parameters from Reference [23].

Parameter	Value	Unit
Electron Energy	0.4 to 1.25	GeV
Peak Current	2.5	kA
Bunch Charge	0.02 to 1.0	nC
Bunch Separation	1 to 25	µs
Bunch Train Length	≤ 800	µs
Bunch Train Rate	10	Hz
Undulator Period	31.4	mm
Undulator Parameter	0.7 to 1.9	
Segment Length	2.5	m
Segment Count	12	
Photon Wavelength	4 to 90	nm
Pulse Energy	1 to 500	µJ
Pulse Duration	10 to 200	fs (FWHM)
Spectral Width	0.5 to 2	% (FWHM)

3.2 Reaction Microscope

The Reaction Microscope (Remi) [51] allows measuring the momenta of charged fragments of an ionization reaction. Although there are not only the reactants for one single reaction inside the Remi, it is still possible to assign products that belong to the same reaction. This is done through coincidence measurement and by applying momentum conservation, as the sum of momenta of all products must be equal to the sum of the reactants' momenta. This technique is known as recoil ion momentum spectroscopy (RIMS). The principle of coincidence measurement requires that it is very unlikely to fulfill momentum conservation by chance. From this follows a requirement to the resolution power for single momenta in order to separate false coincidences from correctly assigned ones. It is necessary to have a sufficiently high signal-to-noise ratio, as noise originating from undesired reac-

tions or just from the measurement electronics are the main sources of wrong coincidence assignments. Measuring the momenta with a Remi is done by extracting charged particles from the reaction volume by homogeneous electric and magnetic fields parallel to the spectrometer axis onto position- and time-resolving detectors (see Figure 3.3). When using a pulsed projectile,

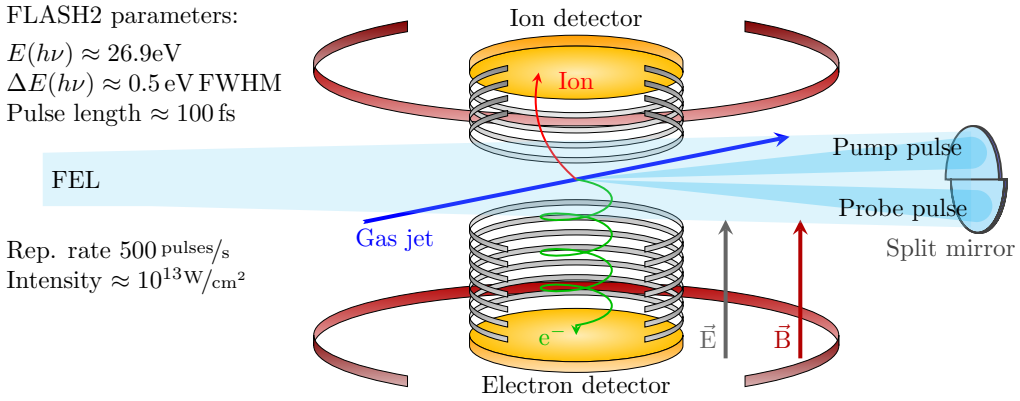

Figure 3.3: Schematic of the setup used for experiments in this thesis. The unfocused FEL crosses the Remi from left to right and is focused back into the gas-jet target. Ions and electrons created from the target are guided to time- and position-sensitive detectors by homogeneous electric and magnetic fields. A time delay can be introduced with the split focusing mirror. Adapted from Reference [45].

the timing interval can be used as a trigger to calculate the time-of-flight to the detector. Combined with the incident position on the detector, one can reconstruct the initial momentum right after the reaction. Naturally, this is best suited for reactions, where all products are charged. But it also possible to infer the momentum of one neutral particle from the other products momenta. Detailed description of the measurement principle can be found in Reference [51].

There are quite different implementations of Remis, in order to allow combinations with different projectiles or targets. In the following the setup used for experiments in this work will be briefly described. For more detailed descriptions, see Reference [38, 45].

The neon target is produced by supersonic expansion of gas through a thin nozzle into the vacuum. Firstly, this allows bringing a target into the spectrometer from some distance without adding materials close, which would disturb the extraction fields. Secondly, the gas jet is cooled in transverse direction by the supersonic expansion. This improves the experimental resolution of momenta transverse to the jet direction. This is also known as

cold target RIMS (COLTRIMS).

The projectiles are intense femtosecond pulses of XUV photons provided by FLASH2 (see Section 3.1). The unfocused beam first crosses the target area and is then focused back into the gas-jet by a split multilayer focusing mirror (see Figure 3.3). The upper part of the mirror can be moved relative to the lower part by piezo elements in order to introduce a time delay of up to $\pm$ 2.5 ps with a resolution of 4 as between the two parts of the pulse reflected from the two halves. As multilayer mirrors are quite sensitive to the photon energy [20], one has to choose and insert the two mirror-halves appropriate to the specific experiment.

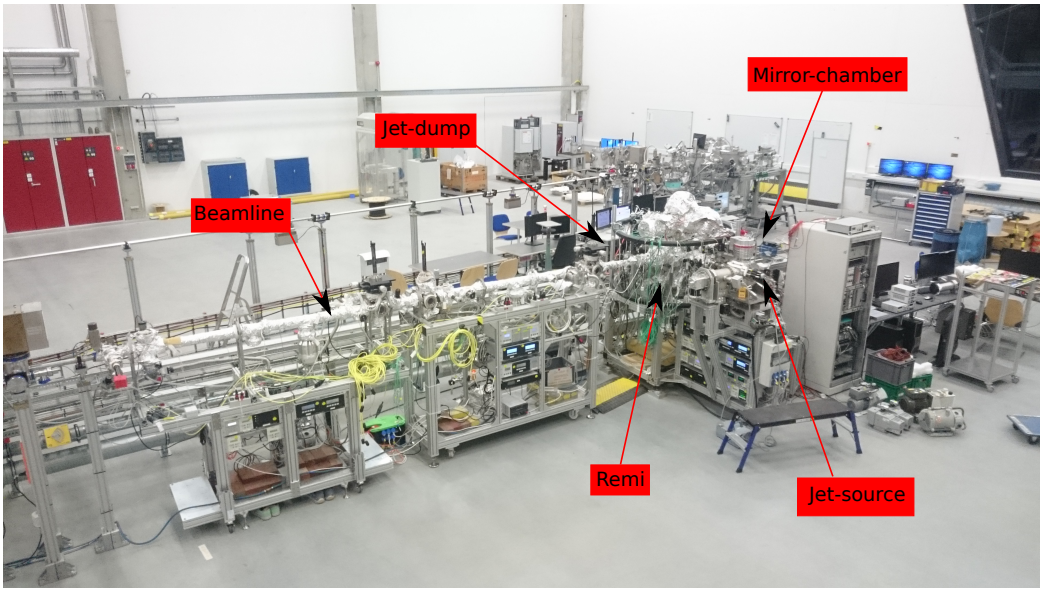

Figure 3.4: Photograph of the Remi beamline at FLASH2.

3.3 Diagnostics

The statistical nature of the SASE process dictates to record and analyze pulse properties on a single-shot level. It is important, that diagnostics are implemented in a non-destructive way, i.e. that they do not, or at least not significantly, alter the pulse before it has arrived at the experiment. If the experiment itself does not alter the pulse it is also possible to do destructive measurements afterwards. For this purpose three different tools are available at the Remi beamline at FLASH2. Firstly, the Gas Monitor Detectors (GMD) for determining the total pulse energy. Secondly, the total pulse energy is observed through a photo-current produced on the focusing

mirror. And thirdly, the Online PhotoIonisation Spectrometers (OPIS) for measuring the mean photon energy of the pulse. The first and third are built into the beam path common to all beamlines at FLASH2.

3.3.1 Gas Monitor Detector (GMD)

The design and capabilities of Gas Monitor Detector (GMDs) are discussed in References [49, 50] and will be summarized briefly. A schematic is shown in Figure 3.5.

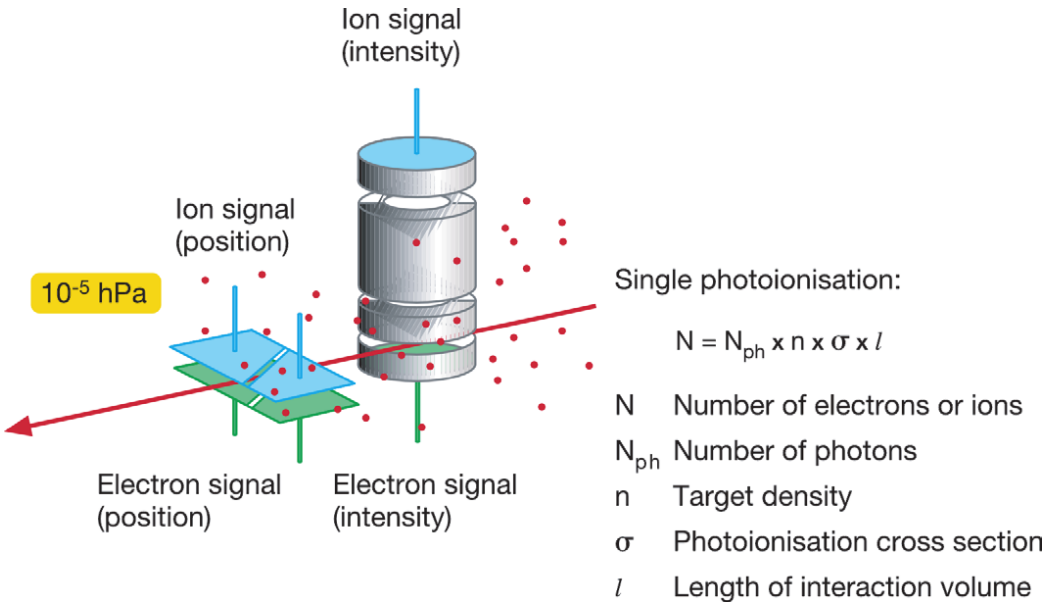

Figure 3.5: Schematic of the GMD. The FEL beam passes along the red arrow and produces ions and electrons from thin gas in the detector chamber. The charged particles are accelerated towards electrodes by electric fields. The total charge collected by those is converted to the number of photons using reference values. Figure taken from [50].

GMDs consist of two seperate devices using the same target gas. Firstly there is a pair of Faraday cups collecting the charge of ions and electrons. Secondly there is a pair of deflection plates, which are used to determine the beam position.

In contrast to traditional ionization chambers, the gas pressure is chosen to be low enough, that almost no secondary ionization processes take place. Typical are values around 10^{-3} Pa or 10^{-5} mbar. This allows to establish a direct linear connection between the charge produced and the number of

photons in the FEL pulse:

$$N_q = N_{\mathrm{ph}} \cdot n \cdot \sigma(\hbar\omega) \cdot l \,, \tag{3.7}$$

where N_q is the absolute charge count of either ions or electrons, N_{ph} is the number of photons in the pulse, n is the target density, $\sigma(\hbar\omega)$ is the ionization cross section as a function of the photon energy and l is characteristic length of the interaction volume. The target density is calculated from measured temperature and pressure of the gas, the ionization cross section is taken from tabulated data and the characteristic length has been calibrated with respect to the light intensity measured by a photo-diode. The total energy E_{pulse} of the pulse is then calculated from the photon energy by

$$E_{\mathrm{pulse}} = N_{\mathrm{ph}} \cdot E_{\mathrm{ph}} = N_{\mathrm{ph}} \cdot \hbar\omega \,. \tag{3.8}$$

As the total absolute charge count has to be equally large for electrons and ions, both can be used to measure the photon count. But technically the ion signal cannot resolve the repetition rate of the FEL during a pulse train and is therefore used to measure only the total energy of the whole train. As the electrons are much lighter and therefore have shorter times of flight towards the Faraday cups, they can be used to resolve the single pulses inside a train.

In the second part of the device, the charge is collected by split electrodes instead of Faraday cups. From the ratio of the charge collected by each half, it is possible to determine the beam position in the transverse beam direction in parallel to the plate electrodes. This information can be used to monitor the beam pointing stability, but is not further analyzed in this work.

At FLASH2 there are two GMDs installed. One inside the tunnel section and another one in the experimental hall.

3.3.2 Photo-Current on Focusing Mirror

The total energy of the FEL can also be measured by observing a photo-current from absorbed photons on the focusing mirror at the FLASH-Remi. Typically, the energy of one photon will be sufficient for multiple electrons to leave the bulk material, so the produced charge will most likely not be proportional to the number of photons. Nevertheless, the amount of charge per pulse will be monotonous as a function of the photon number. This is sufficient in order to calibrate the signal to another observable, which has a known relation to the pulse energy. In this work this is done by counting the ions produced from background gas (e.g. water molecules) inside the Remi and outside the focus region. Therefore, only single-photon ionization is expected for which the cross section is linear to the photon count in the

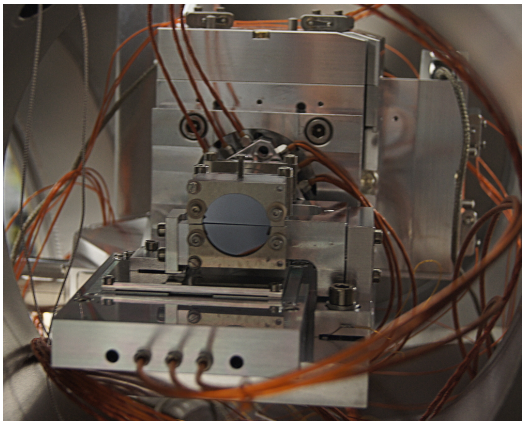

Figure 3.6: Photograph of the back-reflecting focusing mirror. The upper half-mirror can be charged in order to observe the photo-current produced by absorbed photons. Photograph taken from Reference [45].

pulse as long as the process is not saturated, i.e. the remaining neutral atoms or molecules in the volume is high compared to the number of ions. This calibration has to be done with a sufficient amount of statistics collected, but once this is available, the measured relation between the photocurrent and the expected number of ions per pulse can be used to infer the pulse energy from this current on a single-shot basis.

The mirror is negatively charged in order to allow observation of the current via a short drop in voltage. Typically, a few hundred volts are applied. The signal is coupled out via a capacitor, which serves as a high pass. It is then recorded with a fast digitizer, which is also used for recording the detector signals (DC282 digitizer from Agilent, see also Reference [45, pp. 58, 59]).

Additionally to the signal arising from the photons (Figure 3.7a) there is a parasitic signal appearing (Figure 3.7b). This signal originates most likely from the piezo control loop. However, this is not synchronized with the FEL pulse and does not overlap with the true signal most of the time (Figure 3.8a). The ratio between the peak in timing and the uniform distribution suggests a rate for overlapping signals of approximately 10^{-3}. The photocurrent peak is time-gated (see Figure 3.9) and integration yields the observable

$$I_{\mathrm{M}} = \int_{26\,\mathrm{ns}}^{40\,\mathrm{ns}} (U_0 - U(t))\,\mathrm{d}t \approx \sum_{i \in \{i | t_i \in [26\,\mathrm{ns}, 40\,\mathrm{ns}]\}} (U_0 - U(t_i))\,\Delta t\,, \tag{3.9}$$

where Δt is the sampling rate for the recorded voltage $U(t)$. This can then be calibrated in order to get an observable proportional to the photon count,

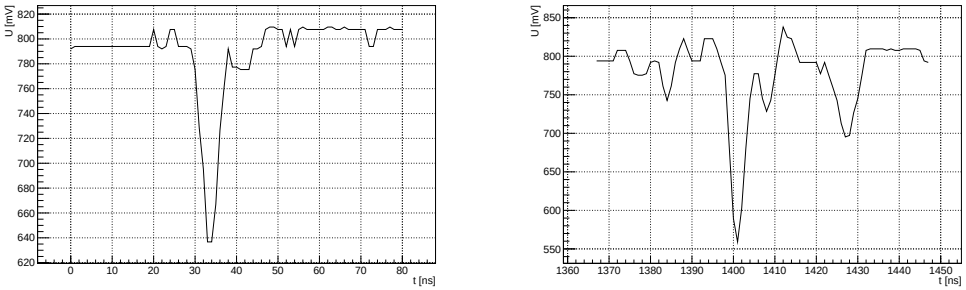

(a) Example signal of the recorded photo-current.

(b) Parasitic signal some time after the signal in (a)

Figure 3.7: Signals acquired from the focusing mirror. For timing of the signals see also Figure 3.8.

i.e. the integrated pulse energy.

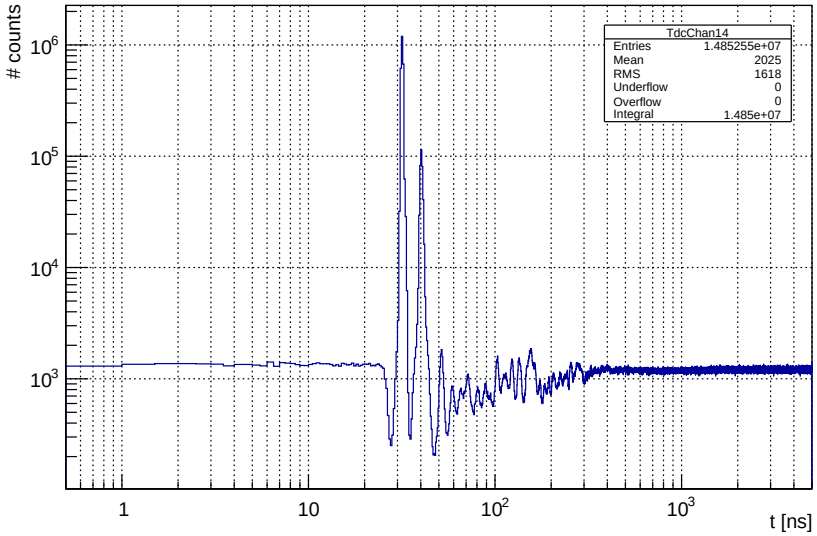

(a) Signal timing histogram with FEL on the mirror.

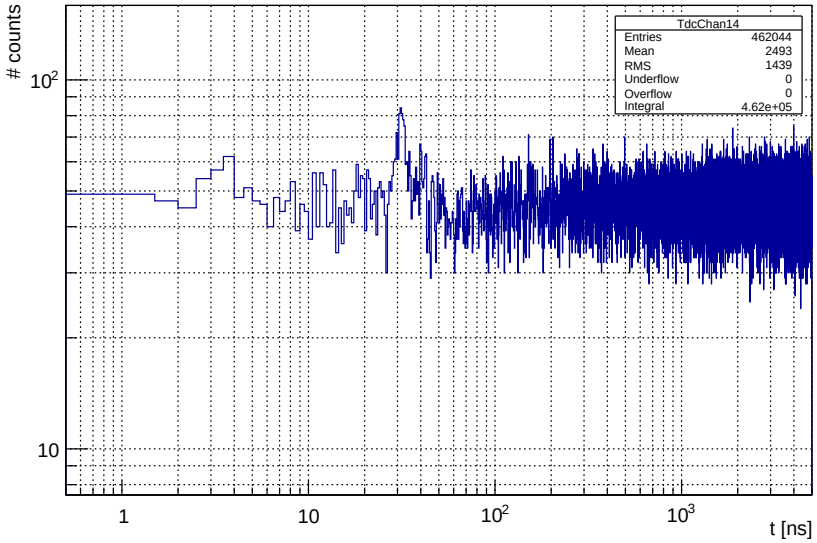

(b) Signal timing histogram without FEL. The FEL-beam was blocked by a shutter in the beamline.

Figure 3.8: Timing histograms of signal peak centers. The parasitic signal appears in a uniform distribution, the photon peak appears always at roughly 35 ns. There are some additional peaks detected after, most probably from decaying oscillation of the signal.

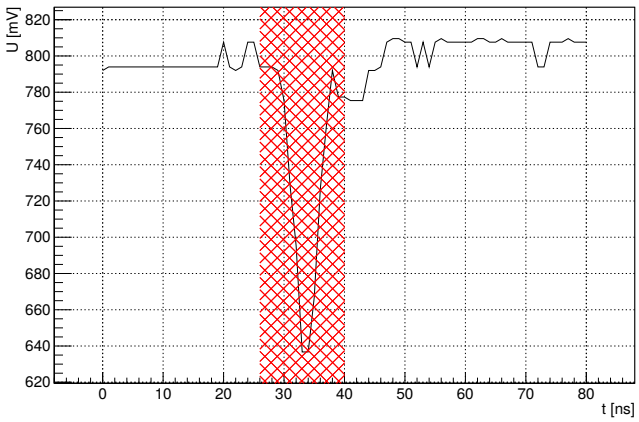

Figure 3.9: Photo signal for a randomly chosen event. The signal is integrated from 26 ns to 40 ns after trigger modulus the pulse-train separation (red filled region). The signal baseline is subtracted before integration.

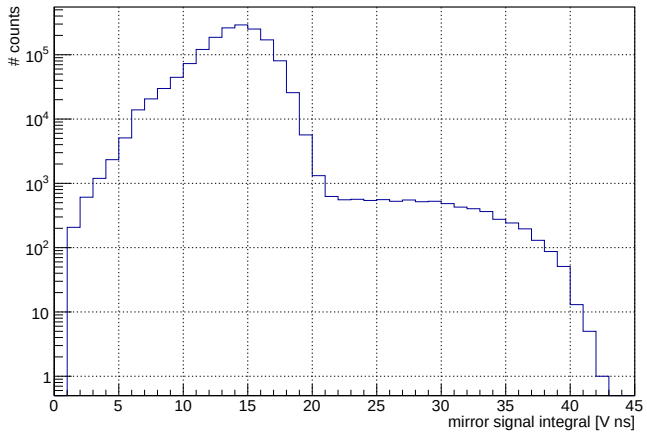

Figure 3.10: Histogram of signal integrals. The main part of the distribution consists of measurements, where the photo-signal can be seperated from parasitic signals. Events with higher absolute value appear, when they can not be seperated. As expected from the timing distribution in Figure 3.8a, these events appear less frequent and can be discarded without loosing a relevant portion of the dataset.

3.3.3 Online Photoionisation Spectrometer (OPIS)

The Online PhotoIonisation Spectrometer (OPIS) was developed to allow live monitoring of the photon spectrum originating from fluctuating SASE FELs. It was first tested as a prototype at FLASH1 and the results from prototype measurements, design and measurement principle are published in Reference [11]. The latter two will be summarized here. The OPIS ver-

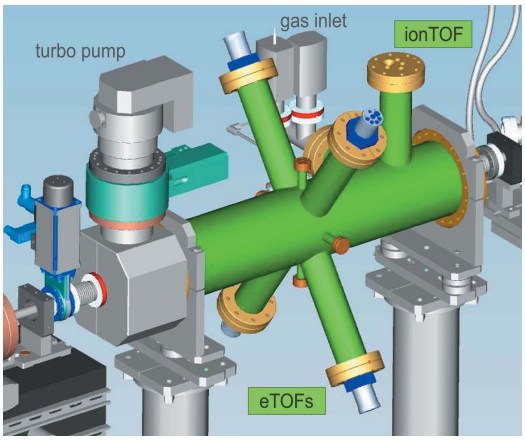

Figure 3.11: CAD drawing of the Online PhotoIonisation Spectrometer. The chamber is filled with a target gas at low pressure. It consists of four electron time-of-flight spectrometers mounted at the magic angle ($\approx 54.7°$) with respect to the FEL polarisation plane (horizontal) and a separate one for ions in vertical direction. Drawing taken from Reference [11].

sion at FLASH2 consists of four electron time-of-flight spectrometers and a separate ion time-of-flight spectrometer (see Figure 3.11). There are two different methods for determining the photon energy of the FEL pulses (see also Figure 3.12).

The target inside the OPIS is a thin gas, similar to the GMD (see Section 3.3.1), in order to minimize the influence of the device on the transmitted beam and to prevent secondary ionization. The gas type has to be chosen according to the photon energy range and intended method.

The first method is to determine the kinetic energy of electrons by measuring their time-of-flight. With a calibrated spectrometer, i.e. the kinetic energy E_{kin} must be known as a function of the time-of-flight, and known binding energy E_{binding}, it is possible to calculate the photon energy E_{ph} from energy conservation:

$$E_{\mathrm{ph}} = E_{\mathrm{binding}} + E_{\mathrm{kin}} \,. \tag{3.10}$$

The electron spectrometers are positioned at the magic angle θ_{m} with re-

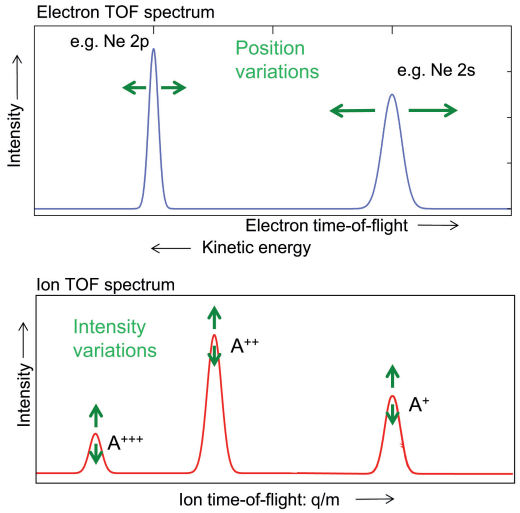

Figure 3.12: Scheme of the measurement methods for the OPIS. In both cases an idealized time-of-flight spectrum is shown. In the upper case electrons are observed. With changing photon energy, the peak positions of electrons from different atomic states shift in time-of-flight direction. In the lower case different ion charge states from the same atomic species are observed. Their peak positions do not change with the photon energy, but the relative height of a specific charge stage changes. Figure courtesy of Markus Braune.

spect to the polarization axis. It is defined by the first root of the Legendre polynomial

$$P_2(\cos\theta_\mathrm{m}) = \frac{1}{2}\left(3\cos^2\theta_\mathrm{m} - 1\right) = 0 \qquad (\theta_\mathrm{m} \approx 54.7^\circ)\,. \tag{3.11}$$

This grants flexibility in choice of target elements and electron states, as the photo-emission rate for linearly polarized light at the magic angle is directly connected to the total rate in dipole approximation [30, pp. 260-261]. It becomes clear from the general form of the differential cross-section

$$\frac{\mathrm{d}\sigma}{\mathrm{d}\Omega} = \frac{\sigma_\mathrm{tot}}{4\pi}\left(1 + \beta P_2(\cos\theta)\right), \text{where} -1 \leq \beta \leq -2\,. \tag{3.12}$$

Here σ_tot is the total cross-section, β is the so called anisotropy parameter and θ is the angle between the light polarization and the momentum of the emitted electron. The anisotropy parameter varies with photon energy, target species and electron states, but is not relevant in this configuration, as $P_2(\cos\theta_\mathrm{m}) = 0$.

As there are two opposing pairs, it is possible to eliminate measurement errors due to a change in beam position and therefore the time-of-flight. With this it is also possible to determine the beam position in both transverse directions. As the conversion relation $E_{kin}(tof)$ is not linear, the resolution for specific electron states depends on the photon energy, so the best choice for the target gas depends on the photon energy. It is possible to do a self-calibration by using electrons originating from Auger decays, when the photon energy is high enough to ionize inner-shell electrons and to produce a vacancy with more energy than the binding energy of the ion.

The second method is based on observing the charge-state distribution of the ions. This is only possible, if one photon carries enough energy to ionize a single atom multiple times. If this is fulfilled, one can find energy ranges, where the yield ratio of two specific charge states R or the mean charge state γ is very sensitive to the photon energy.

$$R = \frac{I(A^{q+})}{I(A^{p+})} \tag{3.13}$$

$$\gamma = \frac{\sum_q I(A^{q+})q}{\sum_q I(A^{q+})} \tag{3.14}$$

Where $I(A^{q+})$ is the absolute yield for ions of the species A with a charge count of q.

In practice it is often easier to use the electron measurement, as it is for

example possible to adapt the conversion function for the electron kinetic energy by means of a retarding voltage if necessary, but the charge state distribution can not be influenced easily by means other than the photon energy.

As one wants to collect enough statistics from the single shot event, the produced space charge will typically not be negligible. A cloud of ions produces a potential well on a macroscopic scale and contributes to another kind of binding energy E_{SC}, which has to be considered for calculating the photon energy

$$E_{\mathrm{ph}} = E_{\mathrm{binding}} + E_{\mathrm{kin}} + E_{\mathrm{SC}} \,. \tag{3.15}$$

The amount of produced charge increases with the pulse energy, but the spatial distribution is not easily accessible. For correct interpretation it will be necessary to model this systematic effect on the determination of photon energies.

4 Data Analysis

The data analysis for this work consists of several procedures. The detected ion signals are sorted into species and charge states using time-of-flight and position conditions (Section 4.1). The mirror photocurrent is calibrated on background gas yields (Section 4.2). The mean photon energy is extracted from OPIS electron spectra and corrected for space-charge effects using the pulse energy as measured by the GMD (Section 4.3). Finally ion yield, photon energy and pulse energy are combined.

The measurements are divided in several runs, with differing parameters (see Table 2). The accelerator setup was not changed, but the photon energy was changed via the undulator gap. The photon-energy setting was corrected by comparison with the optical compact wide-spectral-range XUV spectrometer at FLASH2 [47] during the beamtime. Different metal filters were inserted to adjust the beam intensity.

Table 2: Parameter sets for this analysis.

Parameter	Unit	R728	R729	R730	R731	R732	R733	R734	R735
Wavelength	nm	45.9	46.6	45.2	45.9	46.25	45.55	46.6	45.2
Energy	eV	27.0	26.6	27.4	27.0	26.8	27.2	26.6	27.4
Filter 1	nm Al	402	402	402	402	402	402	402	402
Filter 2	nm Al	200	200	200	402	200	200	402	402

The data collected from the Remi is analyzed using the GENERiC (General Analysis Code for Reaction Microscopes) code implemented in the Go4 [1–3] analysis framework, which is based on ROOT [12]. Procedures are described in detail in Reference [45]. Combining and processing of the data from GMD, OPIS and Remi is done in the Python programming language in the Anaconda distribution [7]. Several Python packages are used, namely for computations numpy [53], bottleneck [27], scipy [33], h5py [16], dask [18] and SPECIFiC [8] and for visualisation matplotlib [31] and seaborn [54].

4.1 Ion Classification

Ion species are classified by imposing time-of-flight and position conditions on the detector signals. The procedure is described in References [38, 45]. Ions from fragmentation of neon dimers are assigned by the coincidence method, through a condition on the sum of the 3D-momentum of both fragments (see Reference [38] or [45]).

Specific to this work is the selection of ions originating from outside the focus area for calibration of the pulse-energy. This is important, as outside the focus region, only single-photon, i.e. linear processes are expected. The time-of-flight conditions for this are shown in Figure 4.1 and spatial conditions in Figure 4.2.

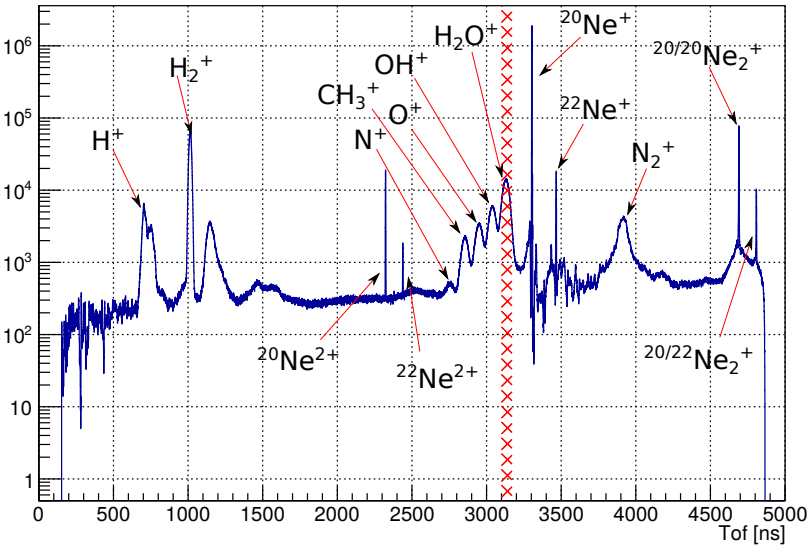

(a) Time-of-flight condition for H_2O^+ (mass-over-charge 18)

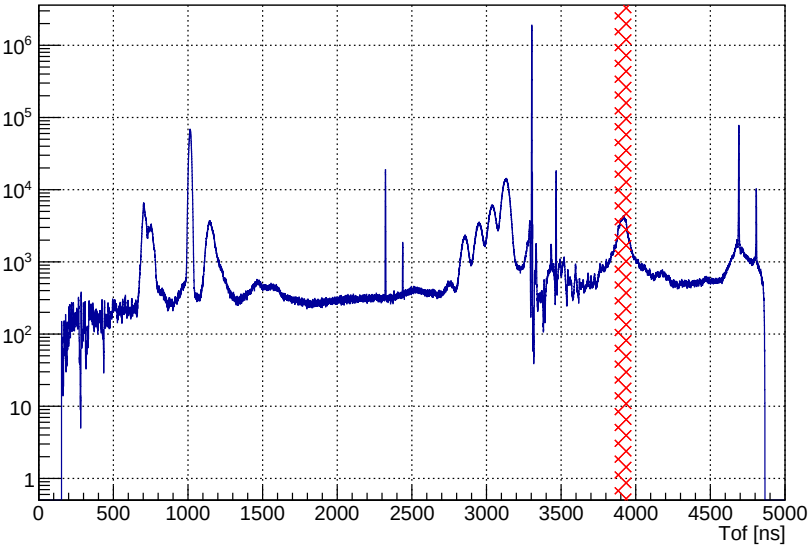

(b) Time-of-flight condition for N_2^+ (mass-over-charge 28)

Figure 4.1: Time-of-flight distribution for detected ions. The target isotopes ^{20}Ne and ^{22}Ne appear singly charged at 3300 ns and 3460 ns. Several species from background gas of mass 14 u to 18 u arrive around 3000 ns. Nitrogen molecules appear at 3900 ns. Several ion species are marked in (a)

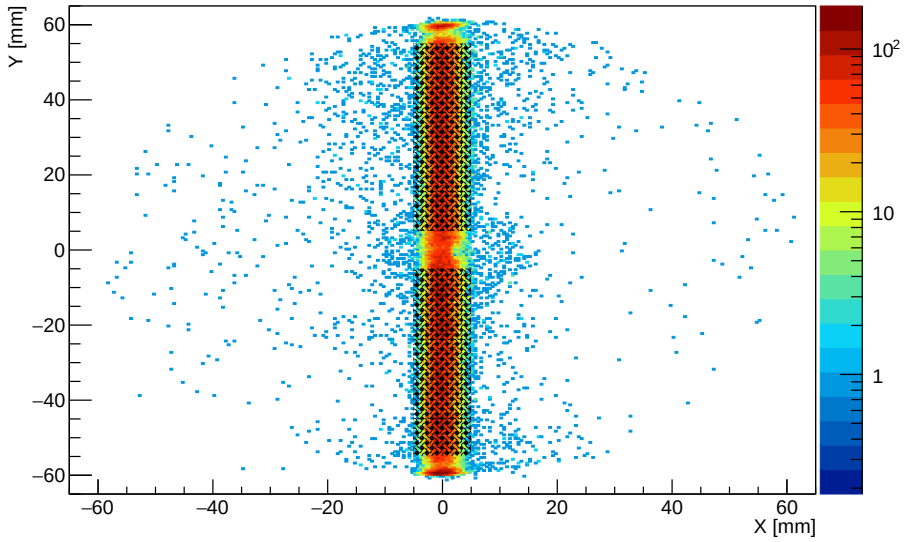

(a) Spatial condition for H_2O^+ (mass-over-charge 18)

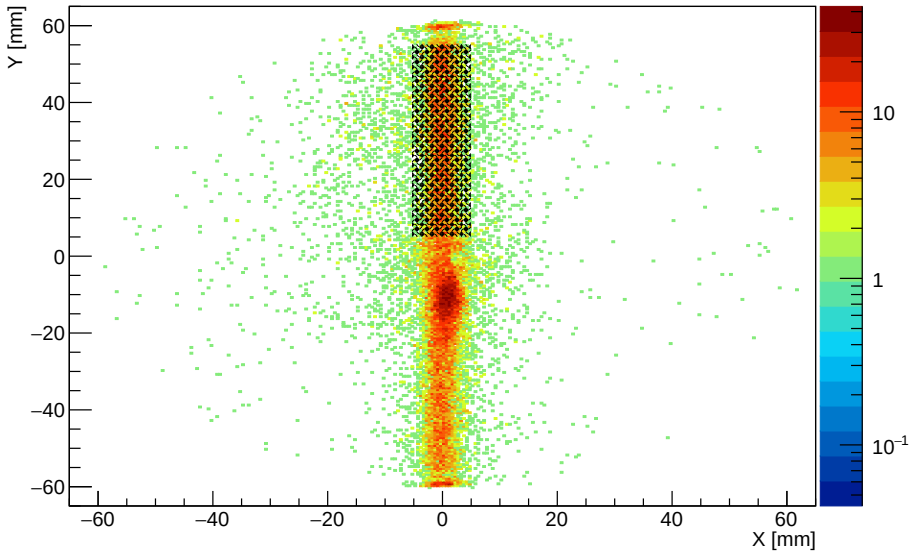

(b) Spatial condition for N_2^+ (mass-over-charge 28)

Figure 4.2: Spatial distribution for detected ions with timings fulfilling the conditions in Figure 4.1. Majority contribution is by singly charged H_2O^+ ions. The crossed regions mark positions considered to be covered by the unfocused FEL beam while being outside the focus region. For nitrogen molecules the lower part is not usable due to a detector artifact at the same timing.

4.2 Photocurrent Calibration

The photocurrent measured, as described in Section 3.3.2, is not linear in the number of photons in the pulse, thus it is necessary to do calibrations. Also small corrections due to ionization cross-sections and mirror reflectivity varying with photon energy have to be done. Those were developed during this work and summarized in the following using molecular nitrogen as an example target species for the calibration.

The calibration is done using the linear relation between ionization yield Y and integrated pulse energy E_{pulse} for single photon ionization:

$$Y(E_{\text{ph}}, E_{\text{pulse}}) = \sigma(E_{\text{ph}}) \cdot n \cdot V \cdot E_{\text{pulse}} \Rightarrow E_{\text{pulse}} \propto Y \Rightarrow E_{\text{pulse}} \equiv c_{\text{ion}}(E_{\text{ph}}) \cdot Y \,. \tag{4.1}$$

Where c_{ion} represents a factor correcting for changes of cross-section, V is the reaction volume and n the number density of atoms. For the runs analyzed here, n is assumed to be constant, as they were recorded in a row. The reaction volume V is not well known, but restricted by a condition on the position on the detector (see Figure 4.2) and with this also constant over the dataset.

The yield of N_2^+ ions is measured as a function of the observable I_{M} derived from the photocurrent on the focusing mirror (see Section 3.3.2). Apart from an constant offset, this relation is close to, but also not perfectly, linear (see Figure 4.3). Therefore, it is approximated by a high-order polynomial. This would fail for extrapolating the calibration to regions with low sampling, however this is not necessary and therefore a polynomial is sufficient.

$$Y_{\text{N}_2}(I_{\text{M}}, E_{\text{ph}}) = \sum_{n=0}^{N} c_i \cdot (c_{\text{mirror}}(E_{\text{ph}}) \cdot I_{\text{M}})^n \,, \tag{4.2}$$

where c_{mirror} is a factor characteristic for the mirror varying with photon energy and c_n are the calibration polynomial coefficients. With Equations 4.1 and 4.2, we get

$$E_{\text{pulse}} \equiv c_{\text{ion}}(E_{\text{ph}}) \cdot \sum_{i=0}^{N} c_i \cdot (c_{\text{mirror}}(E_{\text{ph}}) \cdot I_{\text{M}})^n \tag{4.3}$$

The calibration factors c_i are estimated from the ion rate in the whole measurement. This allows inferring the pulse energy E_{pulse} from the photocurrent observable I_{M} for single pulses. The consistency of this model can be estimated from the variance in the set of measurements. Finding an efficient[2]

[2]Estimators are efficient, when they are unbiased and minimize their variance, where

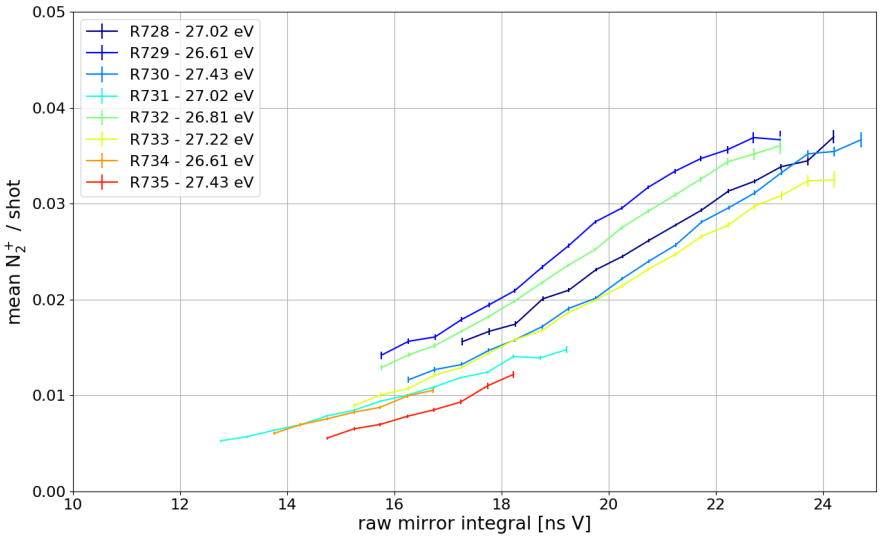

Figure 4.3: Mean molecular nitrogen ion yield vs mirror observable for different datasets neglecting parameter variations. Only data with statistical uncertainty lower than 3% is considered. The average spread of this curves is 13.63% and provides a rough estimate of the systematic error of the calibration.

estimate is usually difficult, so here we will just look at the average ratio between mean and standard deviation. Neglecting the variation of c_{ion} and c_{mirror} the accuracy is in this case 13.63%.

4.2.1 Correcting for Varying Ionization Cross-Section

The photoelectric absorption cross-section changes only slightly with photon-energy, nevertheless it has to be taken into account. The mass attenuation coefficient $\frac{\mu}{\rho}$ (units are [cm^2/g]) is taken from tabulated data [14]. It is connected to the cross-section via

$$\frac{\mu}{\rho} = \sigma \cdot \text{u} \cdot \text{N}_\text{A} \,, \tag{4.4}$$

where u is the atomic unit mass and N_A is Avogadro's constant. A graph of this coefficient versus the photon energy is given in Figure 4.4.

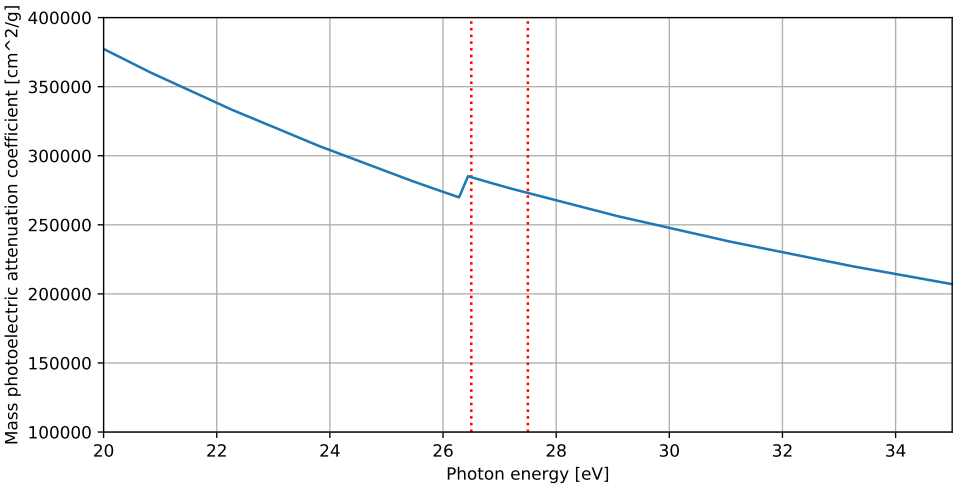

Figure 4.4: The mass photoelectric attenuation coefficient for N_2 molecules as a function of the photon energy. The region relevant for this analysis is marked by the red dotted lines. The data is taken from NIST's *X-Ray Form Factor, Attenuation and Scattering Tables* [14].

For this analysis, the ion rates are scaled by the ratio of the respective cross-section to the lowest, thus removing remaining constants.

$$c_{\text{ion}} = \frac{\sigma_{\text{PE},0}}{\sigma_{\text{PE}}} = \frac{(\mu/\rho)_0}{\mu/\rho} \leq 1 \,. \tag{4.5}$$

minimal variance is provided by the Cramér-Rao bound[24].

With this taken into account, the spread over different measurements is slightly reduced, for molecular nitrogen ions 12.82%, see Figure 4.5.

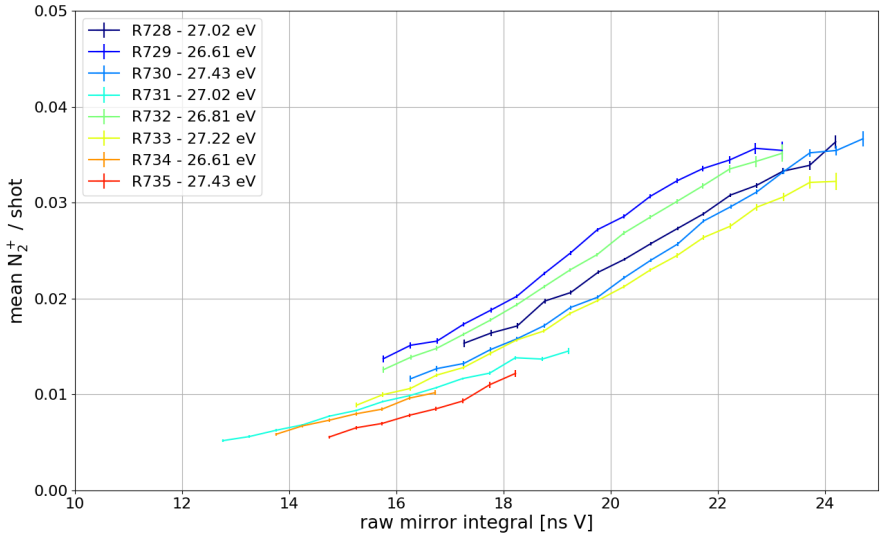

Figure 4.5: Mean N_2^+ ion yield scaled with relative photo-absorption cross-section vs mirror observable for different datasets neglecting parameter variations. Only data with statistical uncertainty lower than 3% is considered. Compared to unscaled relations (Figure 4.3), the spread is slightly reduced as the curves move closer in vertical direction and now at 12.82%.

4.2.2 Correcting for Varying Mirror Reflectivity

The reflectivity of the multi-layer mirror shows a resonant characteristic on the photon energy (see Figure 4.6).

Therefore the observable will show a variation connected to this characteristic. It is assumed that the measured signal is proportional to the absorption $A = 1 - R$ of the mirror, neglecting transmittance. The diagnostic observable is scaled by the absorption relative to the minimum absorption

$$c_{\text{mirror}}(E_{\text{ph}}) = \frac{A_{\text{min}}}{A(E_{\text{ph}})} \leq 1\,. \tag{4.6}$$

This scaling yields good improvement on the accuracy (see Figure 4.7) to 10.50%. When combining this with the scaling of ion yields the overall spread is further reduced to 10.09%, as can be seen in Figure 4.8.

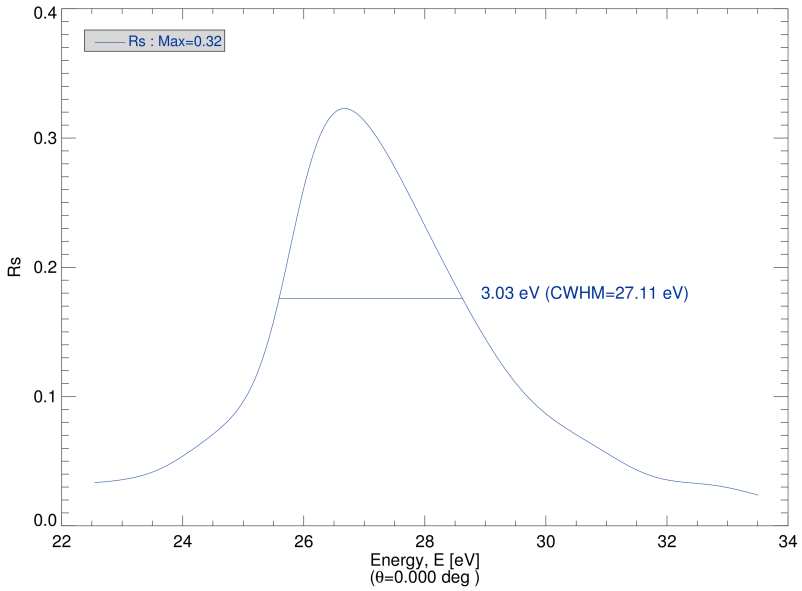

Figure 4.6: Calculated reflectance of the multilayer mirrors used during this work as reported by the manufacturer (Torsten Feigel, optiXfab GmbH, Jena).

Still there is a systematic discrepancy between the two groups of measurements at lower and higher intensities, which might be connected to the choice of filters in the beamline, as those sharing the same filter configuration have better agreement. A possible explanation for the discrepancy might be, that the overall ion detection efficiency also varies with the pulse energy. However, this was not further analysed.

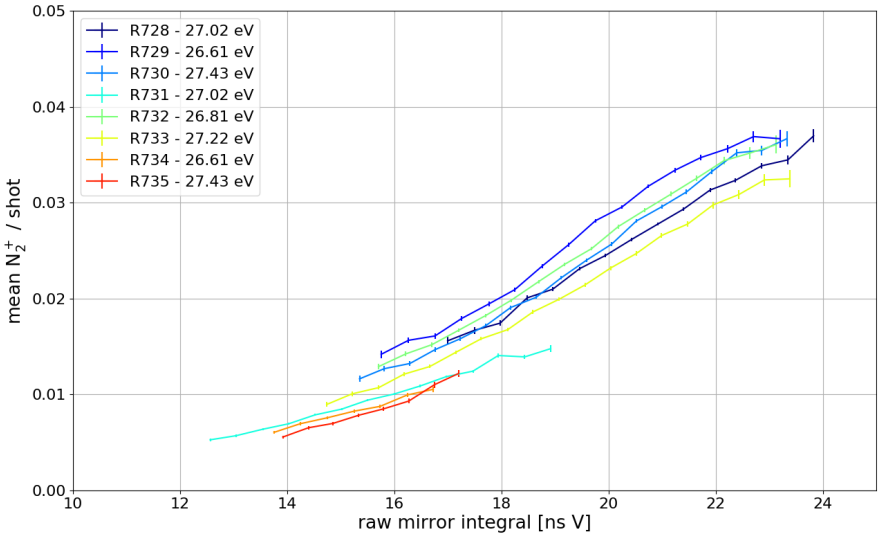

Figure 4.7: Mean molecular nitrogen ion yield scaled with mirror absorption vs mirror observable for different datasets neglecting parameter variations. Only data with statistical uncertainty lower than 3% is considered. Compared to unscaled relation (Figure 4.3), the spread is reduced as the move closer in horizontal direction and is now 10.50%. Compared to the cross-section correction(Figure 4.5), this has larger impact.

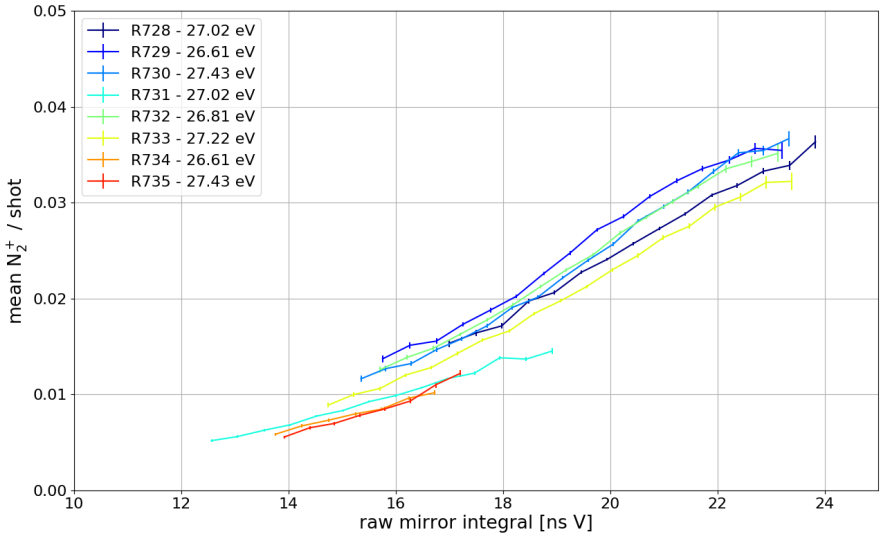

Figure 4.8: Mean molecular nitrogen ion yield scaled with both relative photo-absorption cross-section and mirror absorption vs mirror observable for different datasets neglecting parameter variations. Only data with statistical uncertainty lower than 3% is considered. Compared to the figures with the separate corrections (Figures 4.5 and 4.7), the spread is further reduced to 10.09%.

4.2.3 Signal Calibration – Focus Intensity

The pulse-energy observable is chosen from Equation 4.3, thus the unit of measurement is given by the rate of produced ions of the calibration target species. This energy is valid for the unfocused FEL beam inside the volume accessible to detection with the Remi. In order to translate this to the beam focus, one has to consider the mirror's reflectivity R (Figure 4.6). The relation between unfocused parallel beam and focused intensity is

$$I_{\text{focus}} = R(E_{\text{ph}}) \cdot \left(\frac{d_{\text{parallel}}}{d_{\text{focus}}} \right)^2 \cdot I_{\text{parallel}} \,, \tag{4.7}$$

where d is the beam diameter in the focus or the parallel beam. The change in reflectivity is small, but becomes important for higher powers of the intensity, as the reflectivity contributes with the same power (see Figure 4.9). Due to this, the pulse energy will be scaled for accordingly for analysis of ions produced in the focus.

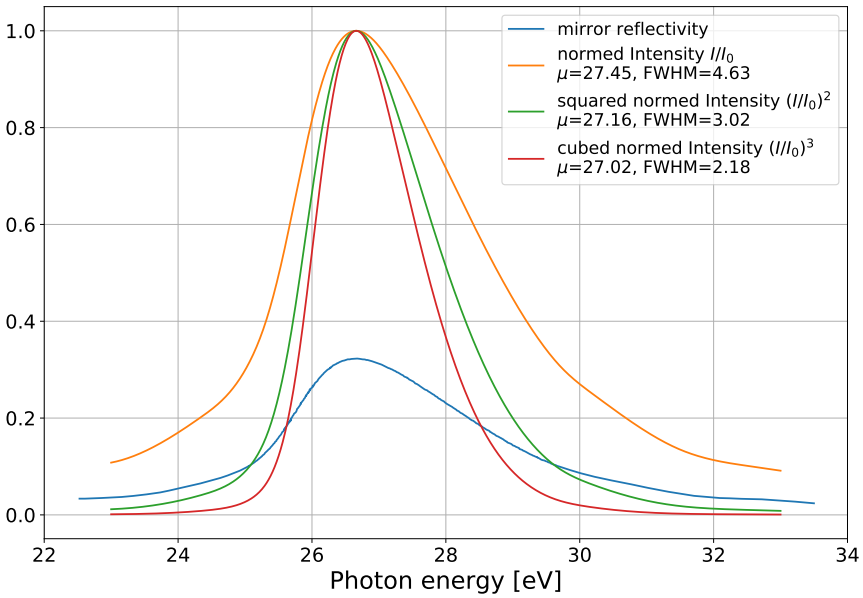

Figure 4.9: Effect of the reflectivity on powers of the intensity at fixed photon energies. Especially for higher orders of the intensity, the change in reflectivity has significant impact.

4.3 Online Photoionization Spectrometer

4.3.1 Conversion from Electron Timing to Photon Energy

The mean photon energy of a pulse is estimated from electron time-of-flight spectra in the OPIS (see Section 3.3.3). This analysis step was performed by Markus Braune [10] and the resulting photon energy from Equation 3.10

$$E_{\mathrm{ph}} = E_{\mathrm{binding}} + E_{\mathrm{kin}}$$

was used for further analysis. For the measurements around 27 eV photon energy, xenon was chosen as a target. Electrons originating from the 5p shell in the ground-state xenon atom ($^1S_0$) have an ionization potential of 12.13 eV. The Xe^+ ion has a fine-structure splitting of the ground state $5p^5$ between the $^2P_{3/2}$ and $^2P_{1/2}$ configurations, where $^2P_{1/2}$ has 1.31 eV additional energy. The next exited state of the ion is $5s5p^6$ $^2S_{1/2}$ with an excitation energy of 11.27 eV, so time-of-flights from other electron states are well separated. For the observed electron kinetic energy this results in a double line close to 14.9 eV with the line splitting mentioned above. Energy level values were taken from Reference [35].

The centre electron energy is determined by fitting the line shape separately on both states. Then the photon energy is calculated from both line positions and finally averaged.

In order to achieve sufficient convergence rates for this fit, it was necessary to use averaged spectra. As FLASH is known to have differing pulse properties depending on the sub-pulse number inside a pulse-train, this averaging is done in a running average over 21 pulse-trains. So the result for pulse with index M in pulse-train N is determined from the averaged spectrum of pulses with index M in the pulse-trains from (N − 10) to (N + 10). This averaging procedure was chosen, as the there are systematic changes of FEL parameters within the pulse trains, which result for example in varying mean intensity with respect to the position of a pulse inside the pulse train. Three examples for single-shot time-of-flight spectra and their running averages can be seen in Figure 4.10.

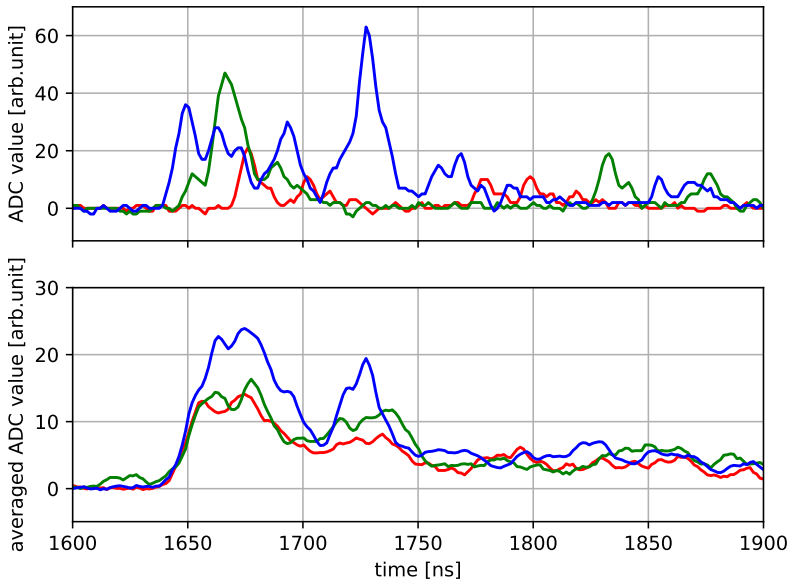

Figure 4.10: Upper: Single-shot electron spectra measured in OPIS. Lower: OPIS electron spectra in running average The shots were chosen randomly.

4.3.2 Space Charge

The resulting mean photon energies as determined in Section 4.3.1 show strong correlations with other pulse characteristics (see Figures 4.11 and 4.12) and thus requires further treatment.

Most notably the correlation between calculated photon- and pulse energy shows clear signature of a space-charge effect. This allows to model the binding energy to the ion charge potential well E_{SC} by fitting a polynomial of high degree to the mean of the uncorrected value per pulse energy interval

$$E_{\mathrm{ph,\ false}}(E_{\mathrm{pulse}}) = E_{\mathrm{binding}} + E_{\mathrm{kin}} + E_{\mathrm{SC}}(E_{\mathrm{pulse}}) = E_{\mathrm{ph,\ true}} + E_{\mathrm{SC}}(E_{\mathrm{pulse}})\,.$$

This mean and the corresponding fit can also be seen in Figure 4.12. As a high-order polynomial fit performs bad for extrapolation, the offset, i.e. the mean of the distribution cannot be estimated by the constant term. Therefore this is determined separately by the median photon energy for all pulses, where the pulse-energy is so low, that no correlation is visible, i.e. below 20 uJ. Here the additional potential from E_{SC} is negligible and we can estimate $\langle E_{\mathrm{ph,\ true}}\rangle = \langle E_{\mathrm{ph,\ true}}\rangle$.

Now for every pulse the expected photon energy $\langle E_{\mathrm{ph,\ false}}(E_{\mathrm{pulse}})\rangle$ is cal-

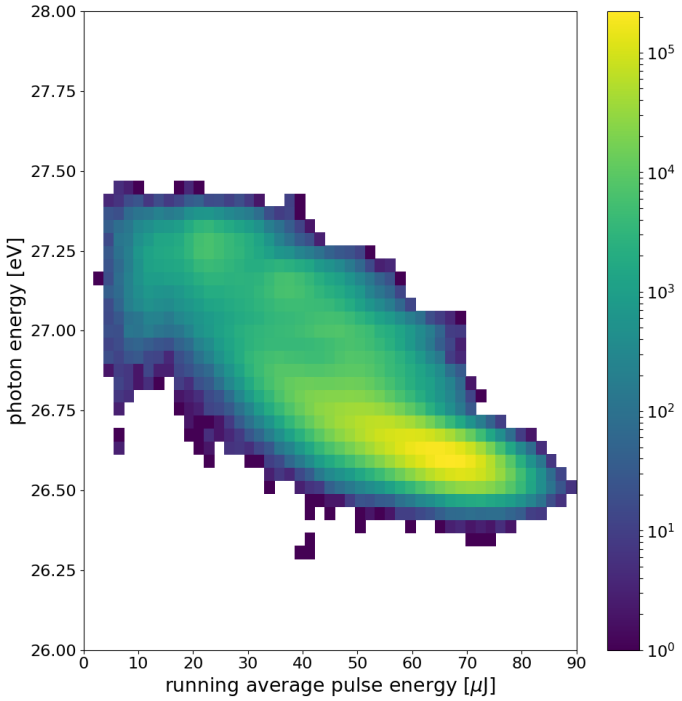

Figure 4.11: Histogram of the common distribution of pulse energy measured with the GMD and photon energy measured by OPIS. At higher pulse energies, the photon energy seems to be reduced. This appears through an macroscopic potential well produced by the collective charge of ions in the spectrometer.

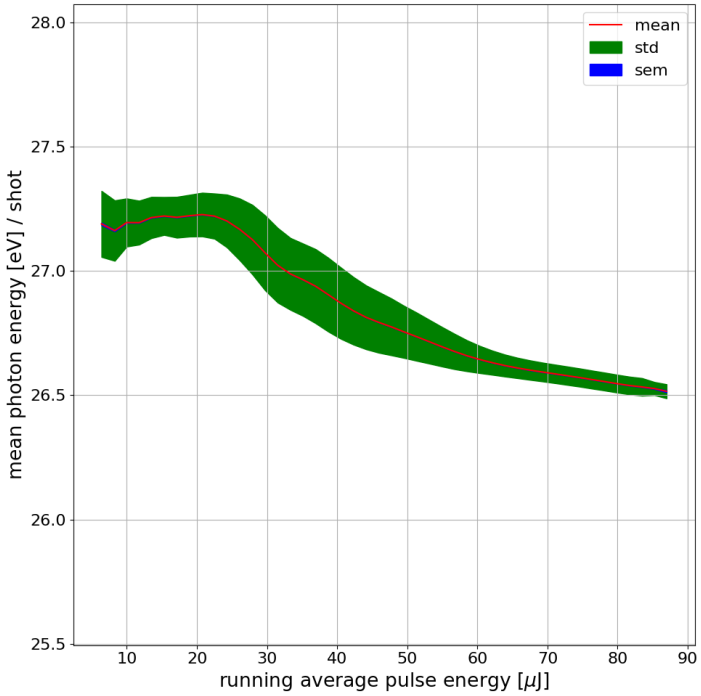

Figure 4.12

Figure 4.13: Distribution statistics of photon energy per pulse energy interval as measured by OPIS and GMD respectively. The trend indicates systematic deviations from the photon energy due to a space-charge potential. Red line: Mean measured photon energy per pulse energy interval. Blue area: One standard error of the mean around the mean. Green area: One sample standard deviation around the mean.

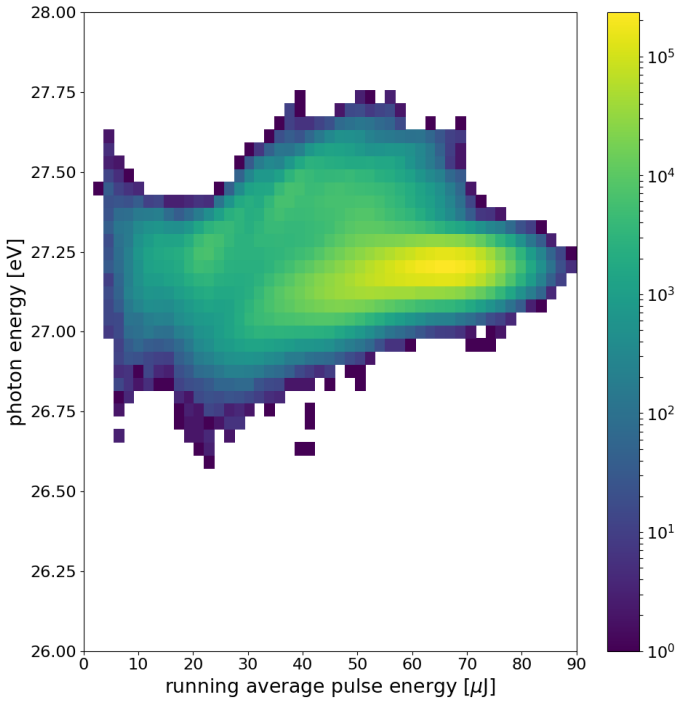

Figure 4.14: Histogram of photon energy corrected for space-charge effects versus pulse energy. There is no average correlation remaining.

culated from the pulse energy as measured by the GMD directly in front of the OPIS and subtracted from $E_{\text{ph, false}}$. Finally the total overall mean energy as estimated above is added to get an estimate of the true photon energy, which is then uncorrelated to the pulse energy (see Figures 4.14 and 4.15).

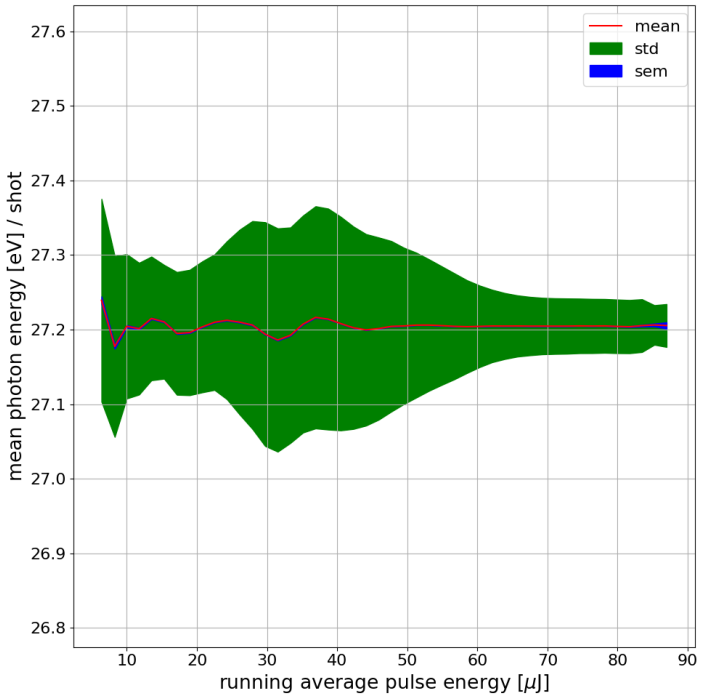

Figure 4.15: Distribution statistics of photon energy corrected for space-charge per pulse-energy interval as measured by OPIS and GMD respectively. The trend indicates systematic deviations from the photon energy due to a space-charge potential. Red line: Mean measured photon energy per pulse-energy interval. Blue area: One standard error of the mean around the mean. Green area: One sample standard deviation around the mean.

4.4 Intensity Scaling

With the calibrated and validated pulse energy available, it is now possible to analyze processes of the target gas in the beam focus. Insight into the reactions can be gained by extracting the power scaling of ion rates versus intensity. For now it is assumed that pulse durations and beam size do not vary much. With this, the intensity is proportional to the pulse energy, as

$$E_{\text{pulse}} = \iint I(t, A)\,\mathrm{d}\,t\mathrm{d}A\,. \tag{4.8}$$

The power scaling of the ion yield Y in absence of saturation effects is expected to follow

$$Y(I) = A \cdot I^n\,. \tag{4.9}$$

This is interpreted to model a process involving n sequential steps, where every step by itself scales linearly with the intensity:

$$Y(I) = \prod_{i=1}^{n} \sigma_i I\,. \tag{4.10}$$

A saturating power law can be modeled with the following class of functions (see also Figure 4.16):

$$Y(I) = A \cdot \frac{I^n/I_1}{\left(1 + (I/I_1)^c\right)^{1/c}}\,, \tag{4.11}$$

where I_1 is the saturation intensity, n is scaling power before saturation and $c > 1$ defines the width of saturation. One finds the two limiting cases

$$\lim_{I \ll I_1} Y(I) = A \cdot \frac{I^n}{I_1} \qquad \text{and} \tag{4.12}$$

$$\lim_{I \gg I_1} Y(I) = A \cdot I^{n-1}\,. \tag{4.13}$$

Deciding between those models can be done with a likelihood-ratio test. For a Gaussian error model, the maximized likelihood $\mathcal{L}$ is

$$\mathcal{L} = \exp(-\frac{n}{2}(\log(2\pi\chi^2) + 1))\,. \tag{4.14}$$

Therefore, the likelihood ratio D is simply given by the inverse ratio of the sum of the squared residuals χ^2 values to the power of the number of sample

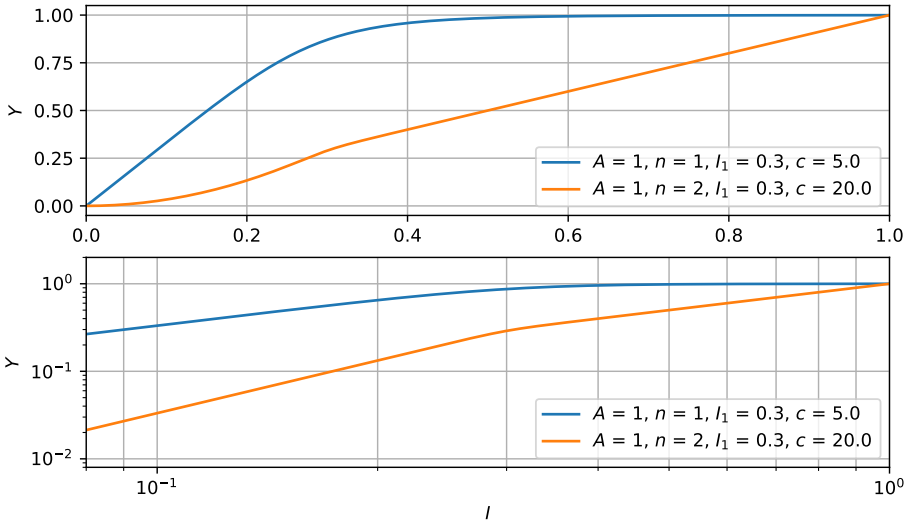

Figure 4.16: Example curves for equation Equation 4.11.

values n

$$D = \frac{\mathcal{L}_2}{\mathcal{L}_1} = \left(\frac{\chi_1^2}{\chi_2^2}\right)^n . \tag{4.15}$$

A more complex model is expected to improve the likelihood significantly in order to be accepted as a replacement of simpler models[3]. In this dataset a ratio limit of $D > 1000$ was chosen to be the decision criterium.

[3]This is known as Ockham's razor[48] (also written as Occam's razor) or the law of parsimony. While correct attribution is actually difficult, as William of Ockham lived around the year 1300, the essential idea appears throughout history and different cultures.

5 Results

In the following, results for the pulse energy calibration (developed in Section 4.2) are compiled in Section 5.1, the analysis of the mean photon energies measured with the OPIS is presented in Section 5.2 and finally the ion rates of neon as a function of intensity are discussed in Section 5.3.

5.1 Pulse-Energy Calibration

For the pulse energy calibration several ion species from background gas can be used. In order to find a good calibration, it is crucial to be in the linear ionization regime. Therefore, ions created in the unfocused FEL beam are used to calibrate the pulse-energy. The calibration for two promising candidates from residual gas are compared in Section 5.1.1. Furthermore, the resulting calibrated data is validated against the measurements available from the GMDs further upstream in the beamline in Section 5.1.2.

5.1.1 Calibration Candidates

Two candidates, namely H_2O^+ and N_2^+, are considered for the calibration. Water ions specifically because they provide the largest amount of statistics. For the central part of the energy distribution, statistics is not critical, but it allows to further extend the limits of values, where measurements can be calibrated. The drawback of this molecule, is that it arrives at similar time-of-flights as OH^+ as well as the very large amount of Ne^+ from the jet (see Figure 4.1), which might have impact on the detector performance and also contributions from incorrect assignments to this molecule. Molecular nitrogen ions however have no other ions in the direct surrounding time-of-flights, but have a factor of about three less counts. Furthermore there is an overlap with a detector artifact both temporally and spatially (see Figure 4.2) so only half of the detection volume can be safely assigned to this channel. Overall this results in six times less accumulated statistics than for water ions.

To decide between those candidates, the variance of the calibrations over the datasets, as described in Section 4.2, is considered. For water ions the variance is 6.63%, for molecular nitrogen ions 10.09%. This difference is probably due to the larger available statistics for water and indicates, that using nitrogen will have a larger variance.

However this is not yet considering a bias towards the correct intensity. In order to compare this, one can check the consistency in the scaling of other ion species from background gas (see for example Figure 5.1). If the

calibration is unbiased, the yield Y of background ions should scale linearly with the calibrated values (see Figure 5.2b), i.e. from Equation 4.9:

$$Y = A \cdot I^n \,, \text{with } n = 1 \,, \tag{5.1}$$

unless this ion species suffers from detection inefficiency. In this case it will scale with $n < 1$. If it, however, scales with values $n > 1$, this indicates, that actually the ion species which was used for calibration was not linearly scaling to the pulse energy and thus provides evidence for systematic bias (see Figure 5.2a). Furthermore the scaling parameter n should not vary significantly in the datasets (see Figures 5.2a and 5.3a).

Finally, but without physical meaning, an important check for consistency, is the condition that ion species used for the calibration of the pulse energy must scale with $A = 1$ and $n = 1$ (see Figure 5.4). This last consistency check is met in both cases. Corresponding comparisons between H_2O^+ and N_2^+ can be seen in Figures 5.1 to 5.4. The scaling models are either Equation 4.9 or, when applicable Equation 4.11:

$$Y(I) = A \cdot \frac{I^n / I_1}{\left(1 + (I/I_1)^c\right)^{1/c}} \,. \tag{5.2}$$

In summary, calibration on molecular nitrogen ions fulfils these criteria and also suggests that counting of water ions is scaling weaker than linear with the pulse energy (see Figure 5.3b). When calibrating on water ions, not only scalings with $n > 1$ occur frequently, but also the scaling varies significantly (see Figures 5.2a and 5.3a).

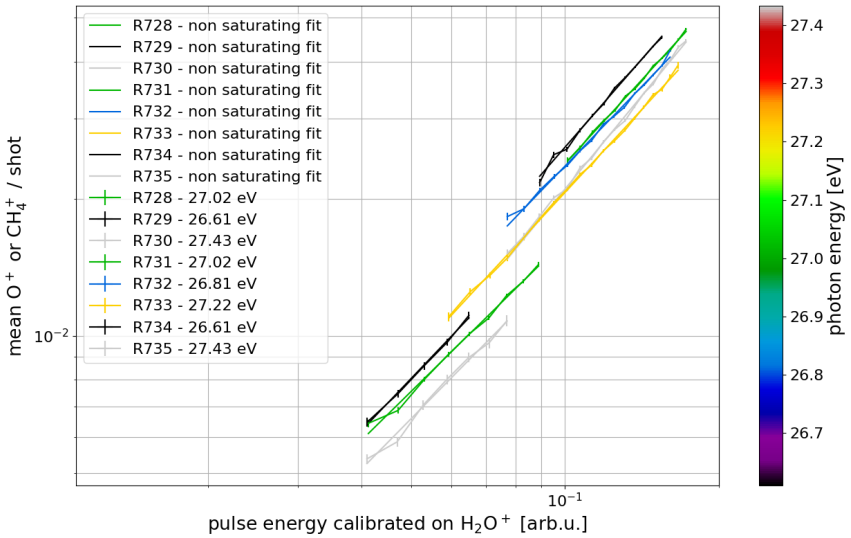

(a) Calibrated on H_2O^+ ion yield.

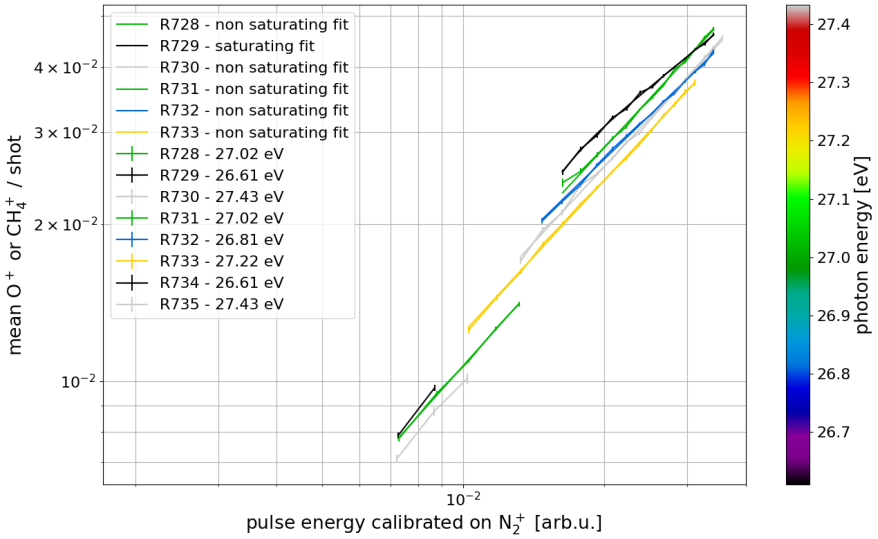

(b) Calibrated on N_2^+ ion yield.

Figure 5.1: Mean ion rate for O^+ (majority contribution from fragmented water molecules) and CH_4^+ (mass-over-charge 16) versus the pulse energy for both calibration candidates. Fit results are shown in Figure 5.2, where model optimization did converge.

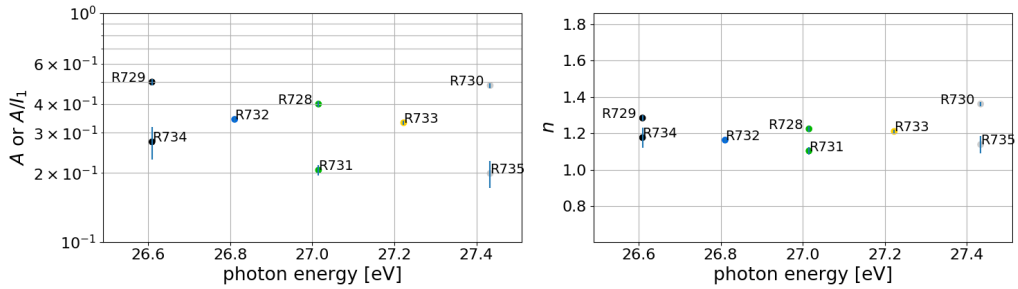

(a) O^+ scaling calibrated on H_2O^+ ion yield.

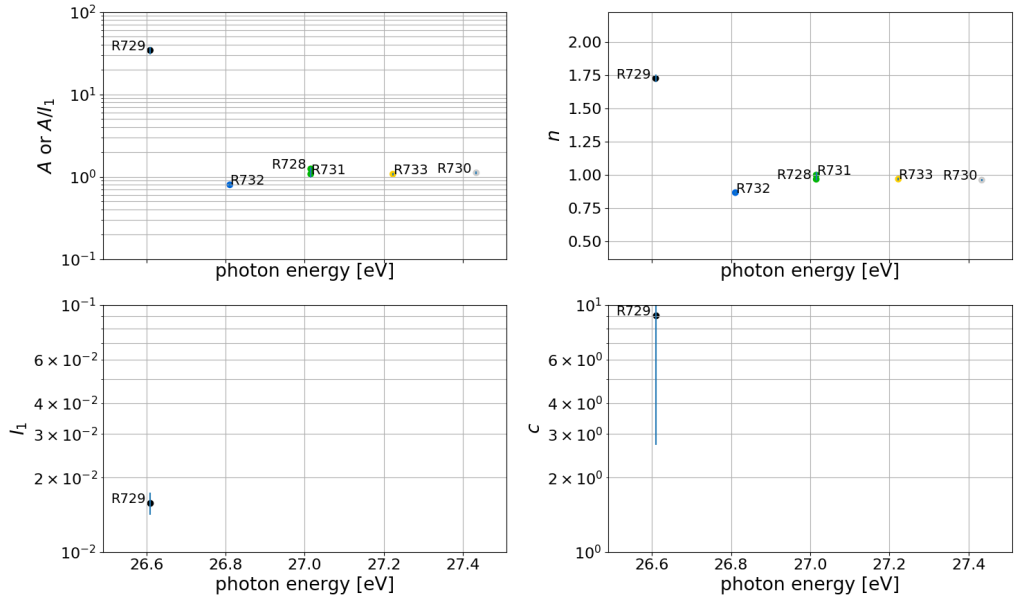

(b) O^+ yield scaling calibrated on N_2^+ ion yield.

Figure 5.2: Scaling of O^+ ion rate. Calibration with water results always in various n above 1, which is not expected. In the molecular nitrogen case all but one run (R729) agree well with $n = 1$ or are slightly below 1. Data-points and fit curves are shown in Figure 5.1. Scaling parameters are according to Equation 4.11 when saturation was modelled, otherwise to Equation 4.9. For better comparison the unsaturated amplitude A/I_1 is depicted in the case of a saturation model.

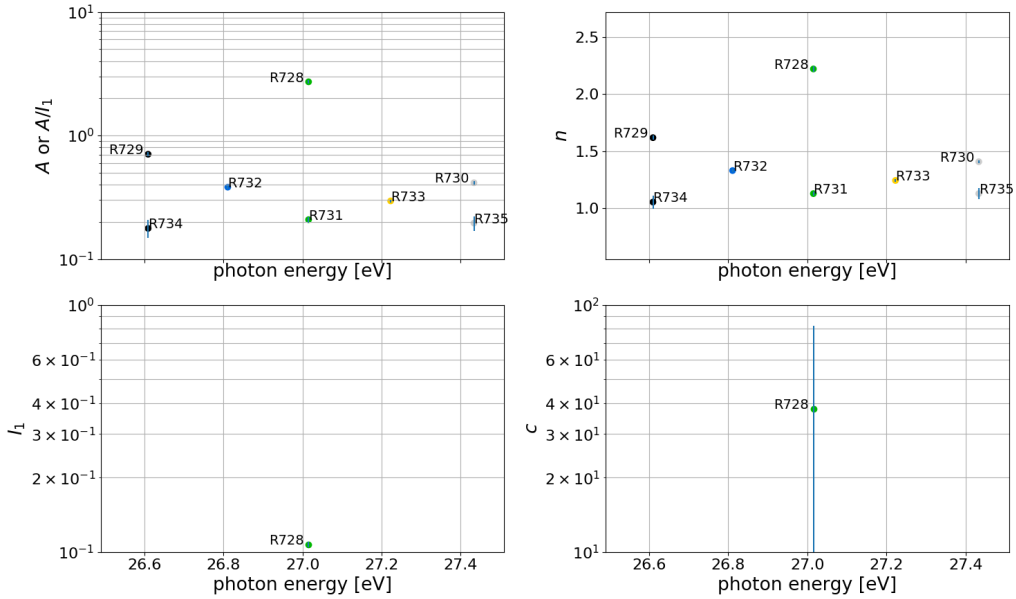

(a) N_2^+ yield scaling calibrated on H_2O^+ ion yield.

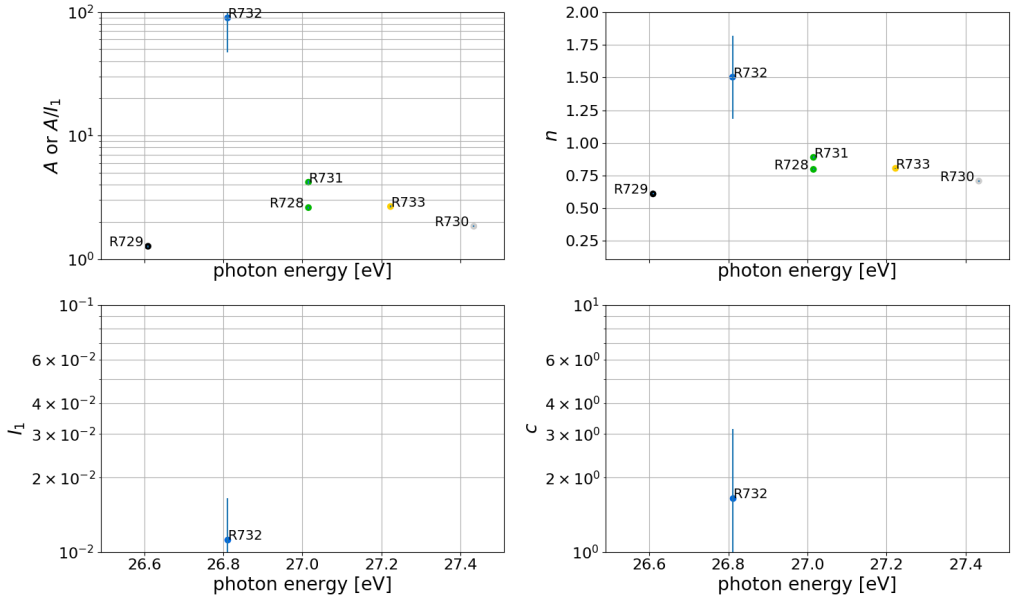

(b) H_2O^+ yield scaling calibrated on N_2^+ ion yield.

Figure 5.3: Yield scaling of the ion used for one calibration against the pulse energy with the other calibration. All runs indicate $n > 1$ for N_2^+ indicating, that calibration with H_2O^+ is not linear to pulse energy. All but one run indicate $n < 1$ for H_2O^+ which is consistent with this. Datapoints and fit curves are not shown. Scaling parameters are according to Equation 4.11 when saturation was modelled, otherwise to Equation 4.9. For better comparison the unsaturated amplitude A/I_1 is depicted in the case of a saturation model.

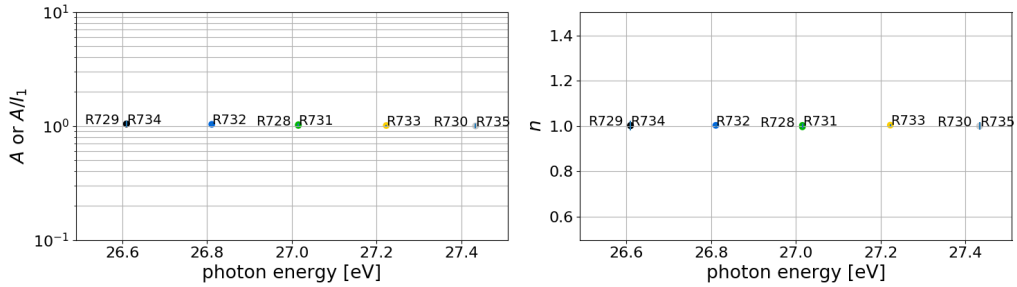

(a) H_2O^+ yield scaling calibrated on H_2O^+ ion yield.

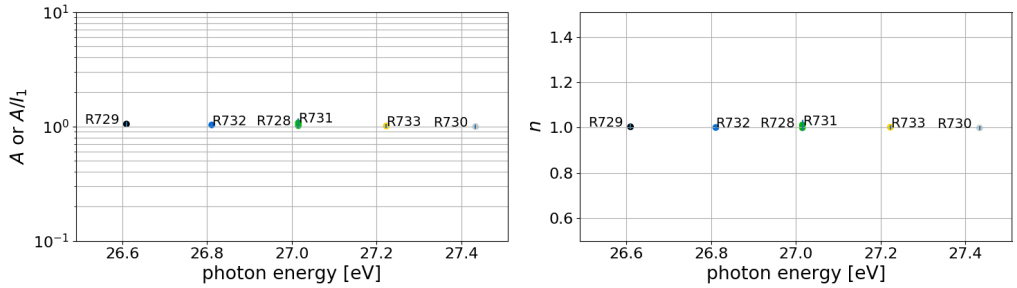

(b) N_2^+ yield scaling calibrated on N_2^+ ion yield.

Figure 5.4: Scaling of the ion rate on the pulse energy calibrated on the same ion species. This has no physical meaning, but must have $A = 1$ and $n = 1$ for consistency. Both variants fulfil this conditions. Data-points and fit curves are not shown. Scaling parameters according to Equation 4.11 when saturation was modelled, otherwise to Equation 4.9. For better comparison the unsaturated amplitude A/I_1 is depicted in the case of a saturation model.

5.1.2 Comparison to GMD

As a validation of this calibration scheme, it is compared to the pulse-energy measurement of the GMDs. The observed quantities need not to correlate strongly on a single-shot basis, as the transmittance in the whole beamline might vary with the beam position and pointing due to several apertures. Nevertheless, mean values of one measurement as a function of the other must be injective, too. This requirement is indeed fulfilled as can be seen in Figure 5.5.

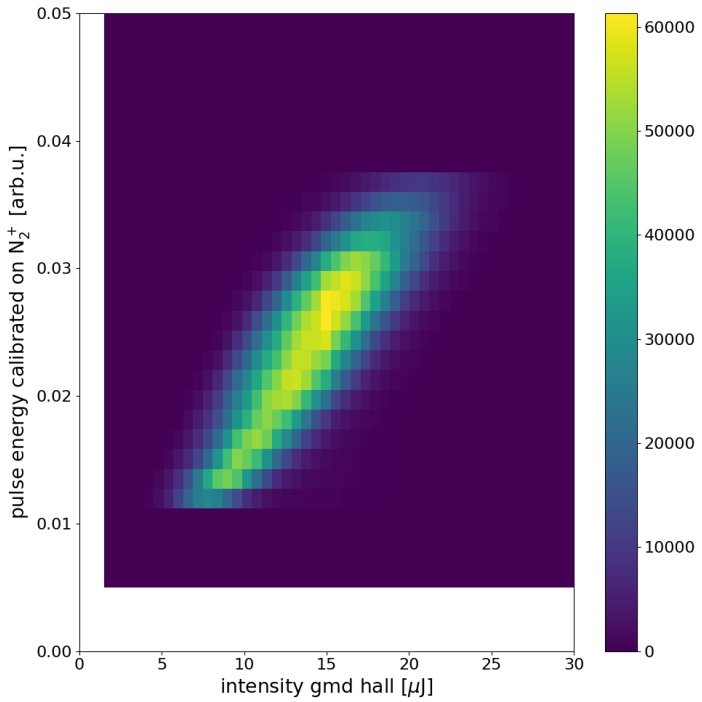

Figure 5.5: Correlation between the tunnel GMD and calibrated mirror signal.

5.2 OPIS Correlations

Although the mean photon energy measured by the OPIS and corrected for space-charge effects is not correlating with the pulse energy (see Section 4.3), there is a significant correlation of the pulse energy with the mean photon energy (see Figure 5.6). Unfortunately this feature dominates also the mean ion yields (see Figures 5.7 and 5.8). This correlation seems counter-intuitive at first, as we removed the inverse correlation, but becomes obvious, when

accounting, that the standard deviation of the mean photon energy decreases as pulse energies increase (see Figure 4.15) until it converges on a minimum value of approximately 0.3 eV. This means, that the distribution of mean photon energies is more tightly concentrated on the overall mean at high pulse energies than at low pulse energies.

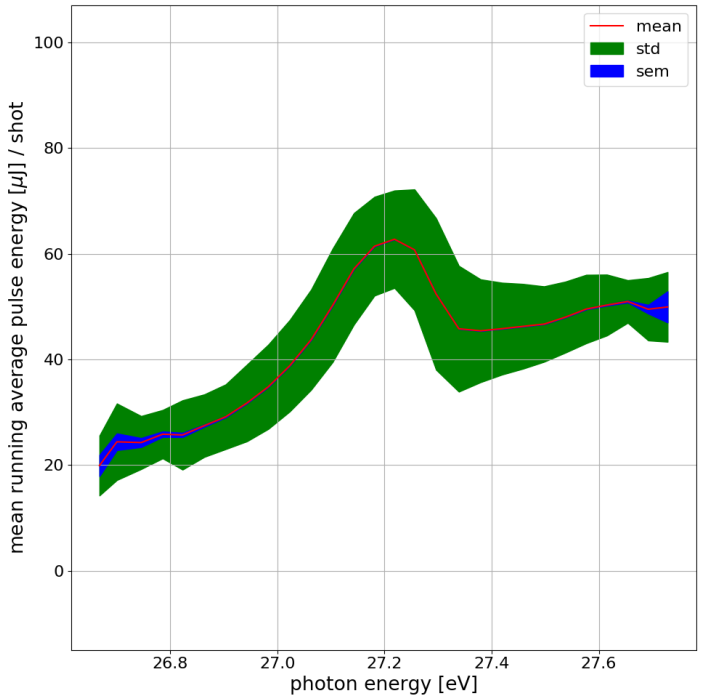

Figure 5.6: Mean pulse energy versus photon energy. Closer to the overall mean photon energy, the mean intensity increases. Red line: Mean measured photon energy per pulse-energy interval. Blue area: One standard error of the mean around the mean. Green area: One sample standard deviation around the mean.

This would be consistent with a picture, where FEL pulses of high total energy actually have a higher count of incoherent sub-pulses contributing to the total pulse. When this is the case, measuring the mean photon energy corresponds to measuring the mean of a random sample from the resonance curve of the undulator interpreted as a probability distribution. The mean of a larger sample will of course converge to the mean of the distribution. This effect is further increased, as only averages of 25 pulses could be analysed. A high average pulse-energy over this 25 pulses means, that most of those pulses have many contributing photon modes. With this, the mean value

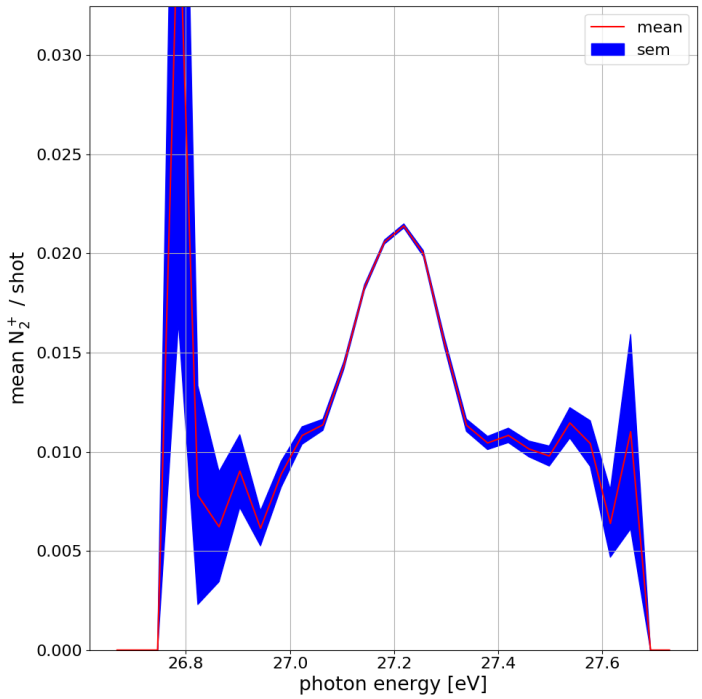

Figure 5.7: Rate of molecular nitrogen ions versus photon energy. It shows the same signature as the pulse energy in Figure 5.6. Red line: Mean measured photon energy per pulse-energy interval. Blue area: One standard error of the mean around the mean.

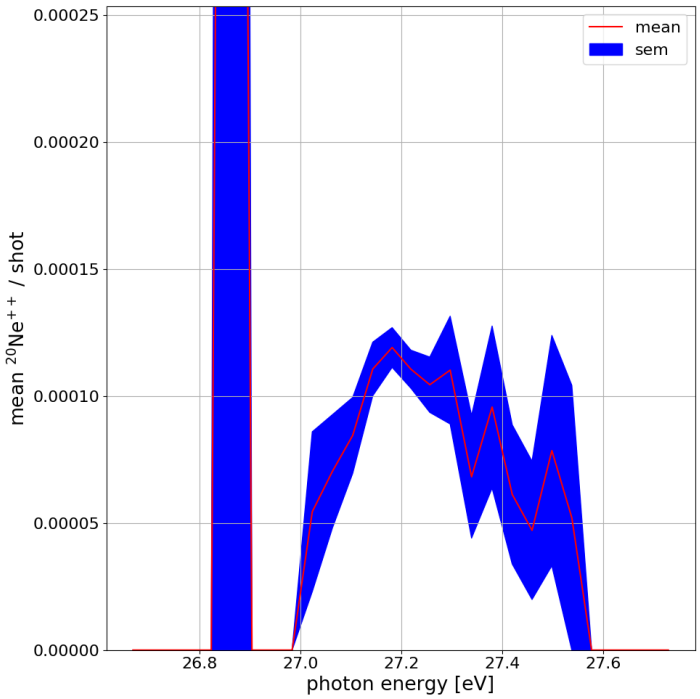

Figure 5.8: Rate of doubly ionized neon versus photon energy. It shows the same signature as the pulse energy in Figure 5.6. Red line: Mean measured photon energy per pulse-energy interval. Blue area: One standard error of the mean around the mean.

becomes less correlated to the actual spectrum of the pulse and further single-shot analysis is not promising any more. Especially as for multi-photon processes the largest part of collected ions is at the high end of the pulse-energy distribution. The full analysis with OPIS data was only performed for run R733, where the photon energy was set to 27.2 eV. This is in very good agreement with the mean value found in this analysis (see Figure 4.15).

5.3 Resonance in Neon Photoionization at 27 eV

The double ionization of neon atoms as well as neon dimers with symmetric fragmentation is analysed against the pulse energy measured by the photocurrent on the focusing mirror calibrated on molecular nitrogen ions (see Section 5.1). Because of the result in Section 5.2, the photon energy is not analysed on a single-shot basis, but only on the overall mean values.

5.3.1 Double Ionization of Neon

The intensity scaling of the yield in double ionized neon is shown in Figure 5.9. The increased yield for photon energies closer to 27 eV provides evidence for resonance enhanced sequential ionization or laser enabled Auger decay taking place and that direct two-photon ionization is negligible (see Section 2.7.1). The scaling exponent n is lower then the expected $n = 3$ for a three-photon process, which indicates that there is already a (partial) saturation present. For run R729, there is another saturation step taking place. This might be happening at low overlap between the resonance and the FEL bandwidth, such that only few photons excite the ions and a comparatively large amount of photons is available for ionization of excited ions. Unfortunately it is unclear, which of the resonant pathways is more relevant. This could be disentangled with more advanced measurements, especially with coincident detection of the photo-electrons, which were not measured in this experiment, as this is challenging and it was not a primary goal of the campaign.

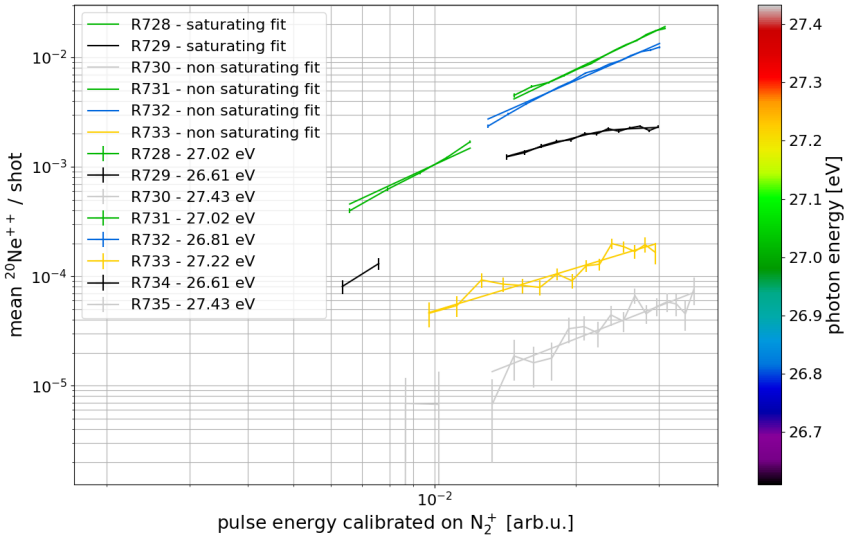

(a) $^{20}Ne^{++}$ ion yield calibrated on N_2^+ ion yield.

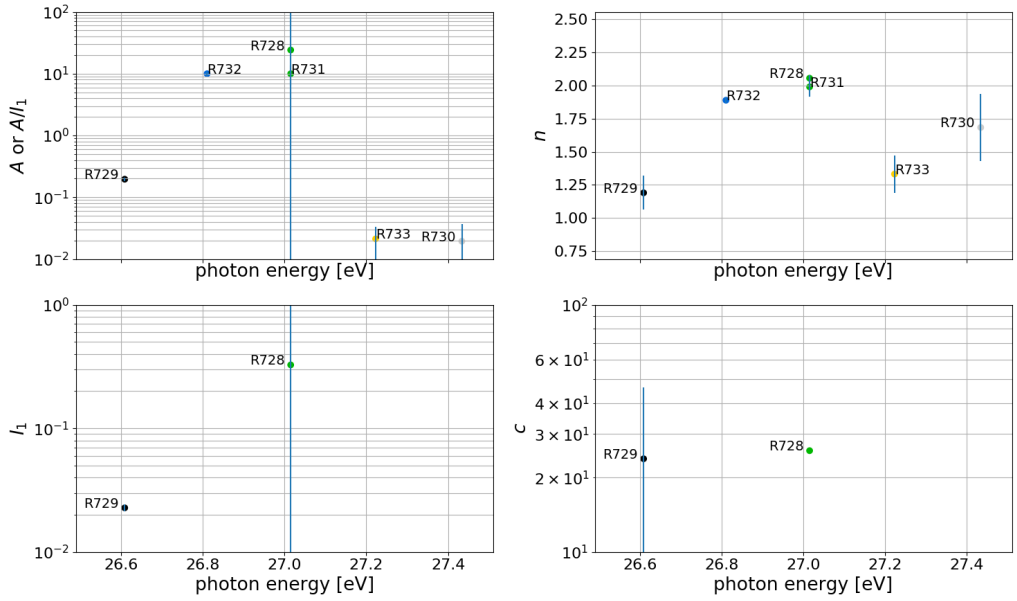

(b) $^{20}Ne^{++}$ yield scaling calibrated on N_2^+ ion yield.

Figure 5.9: Ion yields and scaling parameters for doubly ionized neon. There is strong evidence for a resonant behaviour close to 27 eV in the amplitude. Also the scaling exponent changes from on- to off-resonance energies. (a) Data-points and fit curves. (b) Scaling parameters according to Equation 4.11 when saturation was modelled, otherwise to Equation 4.9. For better comparison the unsaturated amplitude A/I_1 is depicted in the case of a saturation model.

5.3.2 Coulomb-Exploded Neon Dimers

Rates and intensity scaling of Coulomb exploded and in coincidence detected neon dimers are shown in Figure 5.10. The increase in amplitude is not as large, as in the case of double ionization of atoms, but still notable. The scaling with pulse energy is at or slightly below $n = 2$, as expected for a two-photon process. The data-points and fit curves in Figure 5.10a suggest, that the deviation of fit-parameters between R731 (low intensities) and R728 (high intensities) is due to saturation at intermediate pulse-energy.

In summary this is in agreement with ICD being triggered on the resonant 2s-2p transition accompanied with a background due to the direct ionization of both atoms in the dimer. Due to this competing channel, the contrast is expected to be lower, than in the case of double ionization of the monomers, although the absorption cross-section for resonant excitation should not differ for these two cases.

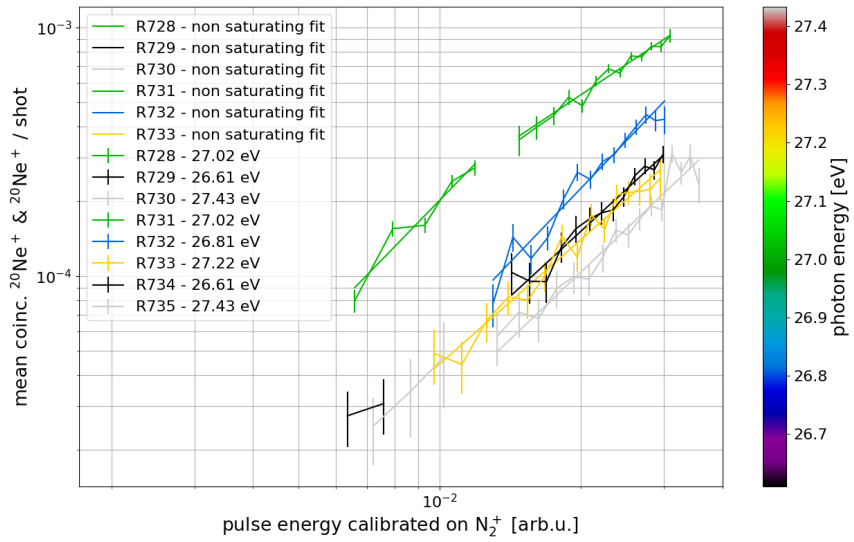

(a) Coincident $^{20}Ne^+$ ion yield calibrated on N_2^+ ion yield.

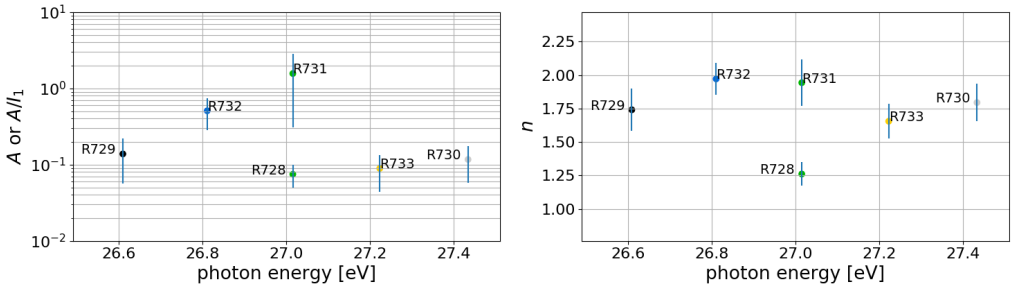

(b) Scaling of coincident $^{20}Ne^+$ ion yield calibrated on N_2^+ ion yield.

Figure 5.10: Coincident ion yields and scaling for double ionization and symmetric fragmentation of neon dimers. Scaling exponents also slightly change with the photon energy. The discrepancy in amplitude and scaling at R728 is due to saturation happening at intermediate intensities, suggested by comparison with the data-points. Ion yields increase around the expected resonance. (a) Data-points and fit curves. (b) Scaling parameters according to Equation 4.11 when saturation was modelled, otherwise to Equation 4.9. For better comparison the unsaturated amplitude A/I_1 is depicted in the case of a saturation model.

6 Summary

It was shown that the ion yield and intensity scaling of three-photon double ionization of atomic neon as well as two-photon double ionization of neon dimers followed by Coulomb explosion varies significantly with the photon energy around the 2s-2p transition at 27 eV in the neon ion. As FLASH2 is operated in SASE mode, its pulse characteristics show large statistical fluctuations and it is thus obligatory to analyse single-shot characteristics when studying processes with non-linear dependence on multiple pulse properties. As this is here the case, diagnostic data from OPIS and the photocurrent on the final focusing mirror at the Remi beamline at FLASH2 have been analysed and several corrections have been developed to extract estimates of the FEL pulse characteristics: total pulse energy and mean photon energy.

The extracted sample distributions were validated on mean values with the help of GMDs for pulse-energy and the undulator resonant frequency for the photon energy. The photon-energy measurement could be validated on average, but due to unfortunate statistical properties, i.e. the mean photon energy converges to the sample mean at high pulse-energies, it could not yet be applied as a single-shot diagnostic. The calibration on the photocurrent could be improved by accounting for both, absorption cross-section of the calibration ion species and the mirror absorption coefficient varying with photon energy. The average sample standard deviation was reduced from 13.63% to 10.09% for calibration on molecular nitrogen ions.

With the resulting calibrated pulse-energy diagnostic data it was possible to model the ion yield with power scaling for different mean photon energies. While this only considers total pulse-energy on a single-shot basis, further insight could still be gained from the scaling models, as amplitudes in non-linear relations are not directly connected to the mean amplitude of the sample. For double ionization of ^{20}Ne, a resonance enhancement between 10^2 and 10^3 was observed, suggesting that competing non-resonant direct non-sequential two-photon ionization does not play a significant role at intensities available here. The rate of Coulomb exploding dimers is increasing only by a factor of approximately 10, but here a non-resonant channel is expected and explains the in smaller enhancement factor.

The photon energy could unfortunately not be fully utilized as a single-shot diagnostic, which would have improved the resolution and thus might also help to identify different ionization channels. Furthermore the corrections on the pulse-energy calibration also depend on the photon energy and would thus be improved. The OPIS wavelength measurement is an important tool, in particular when studying resonant processes, as presented here. Currently, shot-to-shot wavelength information is not available and needs

intense off-line analysis. This allows post-analysis, but no active steering of the experiment while the data are recorded. Therefore, direct online feedback would be desirable for the future. With this results it is possible to state, that at least one of the processes resonance-enhanced sequential ionization or laser-enabled Auger decay takes place in neon around 27 eV photon energy, but they would not be distinguishable. In future experiments this might be possible by also measuring the photo-electrons in coincidence with the ions.

References

[1] J. Adamczewski, M. Al-Turany, D. Bertini, H.G. Essel, N. Kurz, S. Linev and M. Richter. "Go4 on-line monitoring". In: *IEEE Transactions on Nuclear Science* 51.3 (June 2004), pp. 565–570. DOI: 10.1109/tns.2004.828632 (cit. on p. 35).

[2] J. Adamczewski-Musch, H. G. Essel and S. Linev. "Online Object Monitoring With Go4 V4.4". In: *IEEE Transactions on Nuclear Science* 58.4 (Aug. 2011), pp. 1477–1481. DOI: 10.1109/tns.2011.2149541 (cit. on p. 35).

[3] J. Adamczewski-Musch, M. Al-Turany, S. Augustin, D. Bertini, H.G. Essel and S. Linev. *Go4: GSI Object Oriented On-line Off-line system.* Jan. 2017. URL: http://go4.gsi.de (cit. on p. 35).

[4] E. Allaria, R. Appio, L. Badano, W.A. Barletta, S. Bassanese, S.G. Biedron, A. Borga, E. Busetto, D. Castronovo, P. Cinquegrana and et al. "Highly coherent and stable pulses from the FERMI seeded free-electron laser in the extreme ultraviolet". In: *Nature Photonics* 6.10 (Sept. 2012), pp. 699–704. DOI: 10.1038/nphoton.2012.233 (cit. on p. 9).

[5] J. Amann, W. Berg, V. Blank, F.-J. Decker, Y. Ding, P. Emma, Y. Feng, J. Frisch, D. Fritz, J. Hastings and et al. "Demonstration of self-seeding in a hard-X-ray free-electron laser". In: *Nature Photonics* 6.10 (Aug. 2012), pp. 693–698. DOI: 10.1038/nphoton.2012.180 (cit. on p. 9).

[6] P.W. van Amersfoort, R.J. Bakker, J.B. Bekkers, R.W.B. Best, R. van Buuren, P.F.M. Delmee, B. Faatz, C.A.J. van der Geer, D.A. Jaroszynski, P. Manintveld, W.J. Mastop, B.J.H. Meddens, A.F.G. van der Meer, J.P. Nijman, D. Oepts, J. Pluygers, M.J. van der Wiel, W.A. Gillespie, P.F. Martin, M.F. Kimmitt, C.R. Pidgeon, M.W. Poole and G. Saxon. "First lasing with FELIX". In: *Nuclear Instruments and Methods in Physics Research Section A: Accelerators, Spectrometers, Detectors and Associated Equipment* 318.1 (1992), pp. 42 –46 (cit. on p. 8).

[7] *Anaconda Software Distribution*. Computer software. Vers. 2-2.4.0. Nov. 2016. URL: https://anaconda.com/ (visited on 01/09/2017) (cit. on p. 35).

[8] Sven Augustin. *SPECIFiC (Small Python Experiment Concisely Implementing Full GENERiC Calculations)*. private communication. 2017 (cit. on p. 35).

[9] V. Ayvazyan, N. Baboi, J. Bähr, V. Balandin, B. Beutner, A. Brandt, I. Bohnet, A. Bolzmann, R. Brinkmann, O. I. Brovko and et al. "First operation of a free-electron laser generating GW power radiation at 32nm wavelength". In: *The European Physical Journal D* 37.2 (Nov. 2005), pp. 297–303. DOI: 10.1140/epjd/e2005-00308-1 (cit. on p. 8).

[10] Markus Braune. private communication. 2017 (cit. on p. 48).

[11] Markus Braune, Günter Brenner, Siarhei Dziarzhytski, Pavle Juranić, Andrey Sorokin and Kai Tiedtke. "A non-invasive online photoionization spectrometer for FLASH2". In: *Journal of Synchrotron Radiation* 23.1 (Jan. 2016), pp. 10–20. DOI: 10.1107/s1600577515022675 (cit. on p. 31).

[12] Rene Brun and Fons Rademakers. "ROOT – An object oriented data analysis framework". In: *Nuclear Instruments and Methods in Physics Research Section A: Accelerators, Spectrometers, Detectors and Associated Equipment* 389.1-2 (Apr. 1997). New Computing Techniques in Physics Research V, pp. 81–86. DOI: 10.1016/s0168-9002(97)00048-x (cit. on p. 35).

[13] L. S. Cederbaum, J. Zobeley and F. Tarantelli. "Giant Intermolecular Decay and Fragmentation of Clusters". In: *Physical Review Letters* 79.24 (24 Dec. 1997), pp. 4778–4781. DOI: 10.1103/physrevlett.79.4778 (cit. on p. 12).

[14] C.T. Chantler, K. Olsen, R.A. Dragoset, J. Chang, A.R. Kishore, S.A. Kotochigova and D.S. Zucker. *X-Ray Form Factor, Attenuation and Scattering Tables*. Version 2.1. Originally published as Chantler, C.T., J. Phys. Chem. Ref. Data 29(4), 597-1048 (2000); and Chantler, C.T., J. Phys. Chem. Ref. Data 24, 71-643 (1995). National Institute of Standards and Technology, Gaithersburg, MD. 2005. URL: http://physics.nist.gov/ffast (visited on 07/08/2017) (cit. on p. 41).

[15] Henry N. Chapman, Petra Fromme, Anton Barty, Thomas A. White, Richard A. Kirian, Andrew Aquila, Mark S. Hunter, Joachim Schulz, Daniel P. DePonte, Uwe Weierstall and et al. "Femtosecond X-ray pro-

tein nanocrystallography". In: *Nature* 470.7332 (Feb. 2011), pp. 73–77. DOI: 10.1038/nature09750 (cit. on p. 8).

[16] Andrew Collette. *h5py*. URL: http://www.h5py.org/ (visited on 01/09/2017) (cit. on p. 35).

[17] Bridgette Cooper and Vitali Averbukh. "Single-Photon Laser-Enabled Auger Spectroscopy for Measuring Attosecond Electron-Hole Dynamics". In: *Physical Review Letters* 111.8 (Aug. 2013). DOI: 10.1103/physrevlett.111.083004 (cit. on pp. 11, 13).

[18] Dask Development Team. *Dask: Library for dynamic task scheduling*. 2016. URL: http://dask.pydata.org (visited on 11/08/2017) (cit. on p. 35).

[19] Philipp V. Demekhin, Spas D. Stoychev, Alexander I. Kuleff and Lorenz S. Cederbaum. "Exploring Interatomic Coulombic Decay by Free Electron Lasers". In: *Physical Review Letters* 107.27 (27 Dec. 2011), p. 273002. DOI: 10.1103/physrevlett.107.273002 (cit. on p. 10).

[20] J.A. Dobrowolski. "Optical properties of films and coatings". In: *Handbook of Optics*. Ed. by Michael Bass, Eric W. Van Stryland, David R. Williams and William L. Wolfe. 2nd ed. 1995. Chap. 42, p. 42.35 (cit. on p. 24).

[21] D.A. Edwards, ed. *TESLA Test Facility Linac*. Design Report. TESLA 95-01. DESY Print, 1st Mar. 1995 (cit. on pp. 8, 19).

[22] P. Emma, R. Akre, J. Arthur, R. Bionta, C. Bostedt, J. Bozek, A. Brachmann, P. Bucksbaum, R. Coffee, F.-J. Decker and et al. "First lasing and operation of an ngstrom-wavelength free-electron laser". In: *Nature Photonics* 4.9 (Aug. 2010), pp. 641–647. DOI: 10.1038/nphoton.2010.176 (cit. on p. 8).

[23] B Faatz, E Plönjes, S Ackermann, A Agababyan, V Asgekar, V Ayvazyan, S Baark, N Baboi, V Balandin, N von Bargen and et al. "Simultaneous operation of two soft x-ray free-electron lasers driven by one linear accelerator". In: *New Journal of Physics* 18.6 (June 2016), p. 062002. DOI: 10.1088/1367-2630/18/6/062002 (cit. on p. 22).

[24] R. A. Fisher. "On the Mathematical Foundations of Theoretical Statistics". In: *Philosophical Transactions of the Royal Society of London. Series A, Containing Papers of a Mathematical or Physical Character* 222 (1922), pp. 309–368 (cit. on p. 41).

[25] *FLASH - Schematic layout of the facility.* DESY. 27th Aug. 2017. URL: https://flash.desy.de/sites2009/site_vuvfel/content/e66400/infoboxContent156802/FLASH_1_2_layout.pdf (visited on 27/08/2017) (cit. on p. 21).

[26] L. F. Gomez, K. R. Ferguson, J. P. Cryan, C. Bacellar, R. M. P. Tanyag, C. Jones, S. Schorb, D. Anielski, A. Belkacem, C. Bernando and et al. "Shapes and vorticities of superfluid helium nanodroplets". In: *Science* 345.6199 (Aug. 2014), pp. 906–909. DOI: 10.1126/science.1252395. eprint: http://science.sciencemag.org/content/345/6199/906.full.pdf (cit. on p. 8).

[27] Keith Goodman. *Bottleneck. Fast NumPy array functions written in C.* URL: http://berkeleyanalytics.com/bottleneck/index.html (visited on 01/09/2017) (cit. on p. 35).

[28] T. Gorkhover, M. Adolph, D. Rupp, S. Schorb, S. W. Epp, B. Erk, L. Foucar, R. Hartmann, N. Kimmel, K.-U. Kühnel and et al. "Nanoplasma Dynamics of Single Large Xenon Clusters Irradiated with Superintense X-Ray Pulses from the Linac Coherent Light Source Free-Electron Laser". In: *Physical Review Letters* 108.24 (24 June 2012), p. 245005. DOI: 10.1103/physrevlett.108.245005 (cit. on p. 8).

[29] An He, Lingyun Yang and Lihua Yu. "High-Gain Free-Electron Laser Theory, Introduction". In: *Synchrotron Light Sources and Free-Electron Lasers: Accelerator Physics, Instrumentation and Science Applications.* Ed. by Eberhard J. Jaeschke, Shaukat Khan, Jochen R. Schneider and Jerome B. Hastings. Cham: Springer International Publishing, 2016, pp. 119–160. DOI: 10.1007/978-3-319-14394-1_2 (cit. on pp. 9, 18, 19, 21).

[30] Ingolf V. Hertel and Claus-Peter Schulz. *Atoms, Molecules and Optical Physics 1.* Springer Berlin Heidelberg, 2015. DOI: 10.1007/978-3-642-54322-7 (cit. on pp. 11, 33).

[31] J. D. Hunter. "Matplotlib: A 2D graphics environment". In: *Computing In Science & Engineering* 9.3 (2007), pp. 90–95. DOI: 10.1109/MCSE.2007.55 (cit. on p. 35).

[32] D. Iablonskyi, K. Ueda, K. L. Ishikawa, A. S. Kheifets, P. Carpeggiani, M. Reduzzi, H. Ahmadi, A. Comby, G. Sansone, T. Csizmadia and et al. "Observation and Control of Laser-Enabled Auger Decay". In: *Physical Review Letters* 119.7 (Aug. 2017). DOI: 10.1103/physrevlett.119.073203. arXiv: 1705.01812v1 [physics.atom-ph] (cit. on p. 13).

[33] Eric Jones, Travis Oliphant, Pearu Peterson et al. *SciPy: Open source scientific tools for Python*. 2001–. URL: http://www.scipy.org/ (visited on 01/09/2017) (cit. on p. 35).

[34] S. Khan. "Free-electron lasers". In: *Journal of Modern Optics* 55.21 (Dec. 2008), pp. 3469–3512. DOI: 10.1080/09500340802521175 (cit. on p. 18).

[35] A. Kramida, Yu. Ralchenko, J. Reader and and NIST ASD Team. *NIST Atomic Spectra Database (ver. 5.3)*. National Institute of Standards and Technology, Gaithersburg, MD. 2015. URL: http://physics.nist.gov/asd (visited on 29/08/2017) (cit. on pp. 15, 48).

[36] John M. J. Madey. "Stimulated Emission of Bremsstrahlung in a Periodic Magnetic Field". In: *Journal of Applied Physics* 42.5 (Apr. 1971), pp. 1906–1913. DOI: 10.1063/1.1660466. eprint: http://dx.doi.org/10.1063/1.1660466 (cit. on p. 8).

[37] Brian W. J. McNeil and Neil R. Thompson. "X-ray free-electron lasers". In: *Nature Photonics* 4.12 (Nov. 2010), pp. 814–821. DOI: 10.1038/nphoton.2010.239 (cit. on pp. 18, 21).

[38] Severin Morris Meister. "XUV Free-Electron Laser Experiments on Weakly Bound Dimers: Construction of a Water-Dimer Jet Soure and Resonance Enhanced ICD in Ne_2". MSc thesis. Ruprecht-Karls-Universität Heidelberg, 2016 (cit. on pp. 13–15, 17, 23, 35).

[39] N Miyauchi, J Adachi, A Yagishita, T Sako, F Koike, T Sato, A Iwasaki, T Okino, K Yamanouchi, K Midorikawa and et al. "Three-photon double ionization of Ar studied by photoelectron spectroscopy using an extreme ultraviolet free-electron laser: manifestation of resonance states of an intermediate Ar+ion". In: *Journal of Physics B: Atomic, Molecular and Optical Physics* 44.7 (Mar. 2011), p. 071001. DOI: 10.1088/0953-4075/44/7/071001 (cit. on p. 12).

[40] P. Ranitovic, X. M. Tong, C. W. Hogle, X. Zhou, Y. Liu, N. Toshima, M. M. Murnane and H. C. Kapteyn. "Laser-Enabled Auger Decay in Rare-Gas Atoms". In: *Physical Review Letters* 106.5 (Jan. 2011). DOI: 10.1103/physrevlett.106.053002 (cit. on pp. 11, 13).

[41] A Rudenko, Y H Jiang, M Kurka, K U Kühnel, L Foucar, O Herrwerth, M Lezius, M F Kling, C D Schröter, R Moshammer and et al. "Exploring few-photon, few-electron reactions at FLASH: from ion yield and momentum measurements to time-resolved and kinematically complete experiments". In: *Journal of Physics B: Atomic, Molecular*

and Optical Physics 43.19 (Sept. 2010), p. 194004. DOI: 10.1088/0953-4075/43/19/194004 (cit. on p. 8).

[42] Peter Schmüser, Martin Dohlus and Jörg Rossbach. "Ultraviolet and Soft X-Ray Free-Electron Lasers". In: *Springer Tracts in Modern Physics* (2009). DOI: 10.1007/978-3-540-79572-8 (cit. on pp. 18, 20).

[43] K. Schnorr, A. Senftleben, M. Kurka, A. Rudenko, G. Schmid, T. Pfeifer, K. Meyer, M. Kübel, M. F. Kling, Y. H. Jiang and et al. "Electron Rearrangement Dynamics in Dissociating I_2^{n+} Molecules Accessed by Extreme Ultraviolet Pump-Probe Experiments". In: *Physical Review Letters* 113.7 (Aug. 2014). DOI: 10.1103/physrevlett.113.073001 (cit. on p. 8).

[44] K. Schnorr, A. Senftleben, G. Schmid, S. Augustin, M. Kurka, A. Rudenko, L. Foucar, A. Broska, K. Meyer, D. Anielski and et al. "Time-resolved study of ICD in Ne dimers using FEL radiation". In: *Journal of Electron Spectroscopy and Related Phenomena* 204 (Oct. 2015), pp. 245–256. DOI: 10.1016/j.elspec.2015.07.009 (cit. on p. 8).

[45] Kirsten Schnorr. "XUV pump-probe experiments on electron rearrangement and interatomic coulombic decay in diatomic molecules". eng. Mit Zsfassungen in dt. und engl. Sprache. PhD thesis. Heidelberg, Univ., Diss., 2014, 2014, Online–Ressource (213 S.) (Cit. on pp. 11, 23, 27, 35).

[46] A. A. Sorokin, S. V. Bobashev, T. Feigl, K. Tiedtke, H. Wabnitz and M. Richter. "Photoelectric Effect at Ultrahigh Intensities". In: *Physical Review Letters* 99.21 (21 Nov. 2007), p. 213002. DOI: 10.1103/physrevlett.99.213002 (cit. on p. 8).

[47] T. Tanikawa, A. Hage, M. Kuhlmann, J. Gonschior, S. Grunewald, E. Plönjes, S. Düsterer, G. Brenner, S. Dziarzhytski, M. Braune and et al. "First observation of SASE radiation using the compact wide-spectral-range XUV spectrometer at FLASH2". In: *Nuclear Instruments and Methods in Physics Research Section A: Accelerators, Spectrometers, Detectors and Associated Equipment* 830 (Sept. 2016), pp. 170–175. DOI: 10.1016/j.nima.2016.05.088 (cit. on p. 35).

[48] W. M. THORBURN. "OCCAM'S RAZOR". In: *Mind* XXIV.2 (1915), pp. 287–288. DOI: 10.1093/mind/xxiv.2.287 (cit. on p. 55).

[49] K. Tiedtke, J. Feldhaus, U. Hahn, U. Jastrow, T. Nunez, T. Tschentscher, S. V. Bobashev, A. A. Sorokin, J. B. Hastings, S. Möller and et al. "Gas detectors for x-ray lasers". In: *Journal of Applied Physics* 103.9 (May 2008), p. 094511. DOI: 10.1063/1.2913328 (cit. on p. 25).

[50] K Tiedtke, A Azima, N von Bargen, L Bittner, S Bonfigt, S Düsterer, B Faatz, U Frühling, M Gensch, Ch Gerth and et al. "The soft x-ray free-electron laser FLASH at DESY: beamlines, diagnostics and end-stations". In: *New Journal of Physics* 11.2 (Feb. 2009), p. 023029. DOI: 10.1088/1367-2630/11/2/023029 (cit. on p. 25).

[51] J. Ullrich, R. Moshammer, A. Dorn, R. Dörner, L. Ph. H. Schmidt and H. Schmidt-Böcking. "Recoil-ion and electron momentum spectroscopy: reaction-microscopes". In: *Reports on Progress in Physics* 66.9 (Aug. 2003), pp. 1463–1545. DOI: 10.1088/0034-4885/66/9/203 (cit. on pp. 22, 23).

[52] Joachim Ullrich, Artem Rudenko and Robert Moshammer. "Free-Electron Lasers: New Avenues in Molecular Physics and Photochemistry". In: *Annual Review of Physical Chemistry* 63.1 (May 2012), pp. 635–660. DOI: 10.1146/annurev-physchem-032511-143720 (cit. on p. 8).

[53] Stéfan van der Walt, S. Chris Colbert and Gaël Varoquaux. "The NumPy Array: A Structure for Efficient Numerical Computation". In: *Computing in Science & Engineering* 13.2 (2011), pp. 22–30. DOI: 10.1109/MCSE.2011.37. eprint: http://aip.scitation.org/doi/pdf/10.1109/MCSE.2011.37 (cit. on p. 35).

[54] Michael Waskom. *seaborn: statistical data visualization*. URL: http://seaborn.pydata.org/index.html (visited on 01/09/2017) (cit. on p. 35).

[55] L. Young, E. P. Kanter, B. Krässig, Y. Li, A. M. March, S. T. Pratt, R. Santra, S. H. Southworth, N. Rohringer, L. F. DiMauro and et al. "Femtosecond electronic response of atoms to ultra-intense X-rays". In: *Nature* 466.7302 (July 2010), pp. 56–61. DOI: 10.1038/nature09177 (cit. on p. 8).

Danksagung
Ich möchte bei dieser Gelegenheit bei allen bedanken, die mich während der Zeit als Masterstudent begleitet haben und durch ihre Unterstützung diese Arbeit überhaupt erst ermöglicht haben. Besonders danken möchte ich:

- Sven, für Unmengen an Hilfe und Spaß beim Programmieren, Daten analysieren, Karten spielen, Konsolen spielen und in allen sonstigen Lebenslagen.
- Kirsten, für viel guten Rat zur Physik und ihren Überblick am FLASHRemi und dessen Experimente.
- Georg, für seinen unermüdlichen Einsatz und die Geduld mit mir beim Tischfußball.
- Severin, für viele interessante, gemeinsame aber leider (noch) nicht umgesetzte Erfindungen sowie den ein oder anderen geselligen Abend.
- Florian, ebenfalls für den geteilten Erfindergeist sowie die wunderbare Factorio-Fabrik, die hoffentlich noch wachsen wird.
- Robert, für die Gelegenheit in dieser Forschungsgruppe arbeiten zu dürfen und seine lockere Art.
- Claus Dieter, für das viele Wissen zu allem, das er gerne und geduldig teilt.
- Markus Braune, für die Auswertungen zum OPIS.
- dem gesamte FLASH-Team, ohne das die Experimente dort nicht möglich wären.
- Patrizia, für die ein oder andere Tasse Tee, Schokolade oder gar ganzes Frühstück im Büro und sonstige Unterstützung.
- Frans, für unterhaltsame Stimmung sowie die wahlweiße fachlichen oder aber völlig unsachlichen Gespräche im Büro.
- der gesamten restlichen Gruppe, die zum angenehmen und produktiven Klima beiträgt.
- Meiner Familie.

Erklärung:

Ich versichere, dass ich diese Arbeit selbstständig verfasst habe und keine anderen als die angegebenen Quellen und Hilfsmittel benutzt habe.

Heidelberg, den 1. September 2017 .....